TCR-Independent Metabolic Reprogramming Precedes Lymphoma-Driven Changes in T-cell Fate

Rebecca S. Hesterberg[1], Min Liu[2], Aya G. Elmarsafawi[1,3], John M. Koomen[2,4], Eric A. Welsh[5], Stephen G. Hesterberg[6], Sujeewa Ranatunga[7], Chunying Yang[1], Weimin Li[1], Harshani R. Lawrence[7], Paulo C. Rodriguez[8], Anders E. Berglund[9], and John L. Cleveland[1]

ABSTRACT

Chronic T-cell receptor (TCR) signaling in the tumor microenvironment is known to promote T-cell dysfunction. However, we reasoned that poorly immunogenic tumors may also compromise T cells by impairing their metabolism. To address this, we assessed temporal changes in T-cell metabolism, fate, and function in models of B-cell lymphoma driven by Myc, a promoter of energetics and repressor of immunogenicity. Increases in lymphoma burden most significantly impaired $CD4^+$ T-cell function and promoted regulatory T cell (Treg) and Th1-cell differentiation. Metabolomic analyses revealed early reprogramming of $CD4^+$ T-cell metabolism, reduced glucose uptake, and impaired mitochondrial function, which preceded changes in T-cell fate. In contrast, B-cell lymphoma metabolism remained robust during tumor progression. Finally, mitochondrial functions were impaired in $CD4^+$ and $CD8^+$ T cells in lymphoma-transplanted OT-II and OT-I transgenic mice, respectively. These findings support a model, whereby early, TCR-independent, metabolic interactions with developing lymphomas limits T cell–mediated immune surveillance.

Introduction

The Myc oncoprotein is frequently overexpressed in multiple cancer types, including aggressive B-cell lymphomas (1). Myc promotes accelerated cell proliferation and metabolism by inducing genes that orchestrate glucose and amino acid catabolism, as well as genes that control nutrient and metabolite transport (2–7). Increased Myc expression, as well as that of glycolysis-related enzymes and other bioenergetic pathways, are frequently associated with aggressive disease and/or resistance to therapy (8, 9). Although the high metabolic demands of tumors driven by Myc have been proposed to alter immune cells (10, 11), which specific immune cells are impacted and how this might occur remains unclear. Oncogenic Myc also dampens the immunogenicity of cancer cells by suppressing expression of MHC proteins and costimulatory ligands, and by inducing the expression of co-inhibitory ligands such as CD47 and PD-L1 (12–16). Finally, models of Myc-driven B-cell lymphoma have shown that lymphoma cells alter surrounding professional antigen-presenting cells to limit T-cell receptor (TCR) engagement and antitumor activity (17).

T-cell activation following TCR priming leads to upregulation of glycolysis and amino acid metabolism, which fuel both lactate production and the TCA cycle, respectively (18–20). However, in the tumor microenvironment (TME), mitochondrial functions and central metabolic hubs of adaptive immune cells are often suppressed. Previous work suggests persistent antigen exposure and nutrient/metabolite competition cause immune cell exhaustion in the TME (21–27). Many of these investigations have been conducted in solid tumor models and rely on the use of TCR-transgenic T cells that react with a tumor antigen.

Little is known regarding how immune cells are phenotypically and metabolically shaped during early phases of tumor growth and in cancers that are poorly immunogenic. To address this gap, we investigated how Myc-driven B-cell lymphoma regulated adaptive immune responses. Temporal flow cytometry, metabolomic, and expression analyses revealed that lymphoma progression profoundly and selectively affected $CD4^+$ T-cell fate and that early metabolic reprogramming preceded polarization of $CD4^+$ T cells towards Treg and Th1 effector cell phenotypes. Early metabolic changes provoked by lymphoma also occurred in naïve polyclonal T cells and in both $CD4^+$ and $CD8^+$ T cells carrying transgenic TCRs that are incapable of reacting to Myc-driven lymphoma. Thus, TCR-independent, early metabolic reprogramming of T cells is a hallmark of lymphoma progression and immune evasion.

Materials and Methods

Mice

C57BL/6J ($CD45.2^+CD90.2^+$), OT-I, and $CD45.1^+$ mice were purchased from Jackson Laboratories (stock numbers 000664, 003831, and 002014, respectively) and were maintained in the Cleveland lab animal colony. OT-II mice ($CD90.1^+$) were a gift of Dr. Javier Pinilla-Ibarz (Moffitt Cancer Center). Eμ-*Myc* mice (C57BL/6J background, $CD45.2^+$; ref. 28) were from the Cleveland lab animal colony. Both females and males were used for experiments in equal ratios across experimental groups. Sample sizes were at least 3 and no more than 7 mice per cohort. All mice were 6 to 12 weeks old and were

[1]Department of Tumor Biology, H. Lee Moffitt Cancer Center & Research Institute, Tampa, Florida. [2]Proteomics & Metabolomics Core, H. Lee Moffitt Cancer Center & Research Institute, Tampa, Florida. [3]Department of Molecular Medicine, Morsani College of Medicine, University of South Florida, Tampa, Florida. [4]Department of Molecular Oncology, H. Lee Moffitt Cancer Center & Research Institute, Tampa, Florida. [5]Biostatistics & Bioinformatics Shared Resource, H. Lee Moffitt Cancer Center & Research Institute, Tampa, Florida. [6]Department of Integrative Biology, University of South Florida, Tampa, Florida. [7]Chemical Biology Core, H. Lee Moffitt Cancer Center & Research Institute, Tampa, Florida. [8]Department of Immunology, H. Lee Moffitt Cancer Center & Research Institute, Tampa, Florida. [9]Department of Biostatistics & Bioinformatics, H. Lee Moffitt Cancer Center & Research Institute, Tampa, Florida.

Corresponding Author: John L. Cleveland, Department of Tumor Biology, Moffitt Cancer Center and Research Institute, 12902 Magnolia Drive, Tampa, FL 33612. E-mail: john.cleveland@moffitt.org

Cancer Immunol Res 2022;10:1263–79

doi: 10.1158/2326-6066.CIR-21-0813

housed and bred in a specific pathogen-free animal facility. No exclusion criteria of mice were used, and personnel were not blinded. All experiments were approved by the Institutional Animal Care and Use Committee of Moffitt Cancer Center and the University of South Florida.

Lymphoma growth and tissue processing

Two independent Eμ-*Myc* lymphoma transplant models were used, and both were originally derived from B cells isolated from the cervical lymph nodes (LN; processing described below) of Eμ-*Myc* mice having visible lymphoma. B cells were isolated using anti-B220 microbeads (Miltenyi Biotec, 130-049-501). Briefly, single-cell suspensions of lymph nodes were placed in MACS buffer (PBS plus 0.5% FBS [GeminiBio], 0.5% BSA [Sigma], and 2 mmol/L EDTA [Sigma]), and microbeads were added as per the manufacturer's protocol. After 15 minutes of labeling at 4°C, cells were placed in an LS column (Miltenyi Biotec), and the positive selection portion was retained as lymphoma cells. Isolated B lymphoma cells were passaged exclusively *in vivo* into C57BL/6J ($CD45.2^+$) mice via tail vein injection no more than 10 times from the original source and were isolated from the cervical LNs 14 or 21 days after transplanted tumor growth using anti-B220 microbeads as described. Lymphoma cells were viably frozen in 90% FBS with 10% DMSO (Sigma) at −80°C or in liquid nitrogen between passages. Isolation yields were >90% $B220^+$ purity. Lymphoma growth was induced by transplanting 2×10^5 Eμ-*Myc* lymphoma cells in PBS into C57BL/6J, $CD45.1^+$, OT-I, or OT-II mice via tail vein injection.

Spleens, cervical LNs, and/or femurs and tibias were isolated from tumor-bearing mice at Day 7 (Early) and at Day 14 or Day 21 (Late) after Eμ-*Myc* transplant (unless otherwise indicated) or from nontumor-bearing mice. Spleens and LNs were processed by disassociating with a 100-μmol/L cell strainer and a syringe plunger in complete media (RPMI with 10% FBS, 1% nonessential amino acids, 50 μmol/L 2-mercaptoethanol, 1% sodium pyruvate, and 1% pen/strep; all from Thermo Fisher Scientific, except FBS, which was from GeminiBio). Bones were crushed using a mortar and pestle in complete media. Single-cell suspensions of spleens and bone marrow were centrifuged, resuspended in 1 mL of RBC lysis buffer (154 mmol/L NH_4Cl, 10 mmol/L $KHCO_3$, 0.1 mmol/L EDTA in water; materials were all from Sigma) for less than 1 minute, and 10 mL of complete media was added to stop the RBC lysis reaction. The number of splenocytes were then enumerated by trypan blue dye (Thermo Fisher Scientific) exclusion on a Nexcelom automatic cell counter. Cells were then used for cell isolation or other analyses as indicated below.

Blood counts

Blood was collected via submandibular bleed into EDTA tubes (Becton Dickinson) from C57BL/6J mice 7 or 14 days after Eμ-*Myc* lymphoma transplant and from control (nontumor-bearing) C57BL/6J mice. Complete blood counts were then determined using a ProCyte Dx Hematology Analyzer (IDEXX).

Cell isolation

All reagents associated with Pan T-cell or $CD4^+$ T-cell isolation were purchased from Miltenyi Biotech. To isolate Pan T cells or $CD4^+$ T cells, spleens from control (nontumor-bearing) and Eμ-*Myc* lymphoma-bearing mice were dissociated into single-cell suspensions, counted (as described above), and placed in MACS buffer (Miltenyi). Pan T cells and bulk or naïve $CD4^+$ T cells were isolated using immunomagnetic negative selection following the manufacturer's protocol with >90% purity (Miltenyi, 130-104-454, 130-095-130, 130-104-453). For Eμ-*Myc* lymphoma-bearing mice, extra anti-B220 microbeads (~20 μL, Miltenyi) were added to ensure purity, and spleens from Day 14/Late Eμ-*Myc* lymphoma-bearing mice were run through an LD column. All other samples were run through an LS column (Miltenyi). For metabolomics and RNA sequencing (RNA-seq) only, $CD4^+$ T cells from Day 14/Late Eμ-*Myc* lymphoma-bearing mice were subsequently labeled with CD4-PE and anti-PE microbeads (Tonbo, 50-0042-U100; Miltenyi, 130-048-801) and run through a second LS column for positive selection to achieve higher purity (>95%).

To isolate Eμ-*Myc* lymphoma cells for metabolomics, 2×10^5 Eμ-*Myc* lymphoma cells from the sources described above ($CD45.2^+$) were transplanted into $CD45.1^+$ congenic mice. At the indicated time points, spleens were dissociated into single-cell suspensions, as described, and labeled for sorting by FACS with CD45.2 and B220 antibodies as well as DAPI as described below. For control splenic B cells, spleens from nontumor-bearing C57BL/6J ($CD45.2^+$) mice were processed and sorted similarly alongside each sort of cells from lymphoma-bearing mice. Cells were sorted using a BD FACS Aria for viable $CD45.2^+B220^+$ cells and were >95% pure.

Adoptive cell transfer into congenic mice

Two cohorts of $CD45.1^+$ mice served as recipient mice for adoptive cell transfer experiments. One cohort was injected with Eμ-*Myc* lymphoma cells ($CD45.2^+$) and the other served as nontumor-bearing controls. Seven days after Eμ-*Myc* lymphoma transplant, all $CD45.1^+$ mice then received $CD45.2^+$ $CD4^+$ and $CD8^+$ T cells isolated from spleens of control (nontumor-bearing) C57BL/6J mice, using a Pan T Cell Kit (Miltenyi, as described above). The isolated T cells ($CD45.2^+$) were injected via tail vein (5×10^6 T cells) into control (nontumor-bearing) or the lymphoma-bearing $CD45.1^+$ recipient mice. Mice were euthanized 48 hours later, and $CD45.2^+$ T cells were analyzed from single-cell suspensions of splenocytes via flow cytometry as described below.

OVA vaccination

Control (nontumor-bearing) OT-II mice ($CD90.1^+$) and OT-II mice ($CD90.1^+$) bearing Eμ-*Myc* lymphomas 14 days after transplant were euthanized, and $CD4^+$ T cells were isolated from spleens as described. 1.5×10^6 $CD4^+$ T cells were then adoptively transferred into sublethally irradiated congenic C57BL/6J $CD90.2^+$ hosts via tail vein injection (JL Shepherd Mark 1, Model 68A CS-137 Irradiator; 600 RAD, <24 hours prior to tail vein injection). Mice were immediately injected intraperitoneally with 100 μg ovalbumin 323–339 peptide (OVA323–339, Anaspec) and 10 μg lipopolysaccharide (LPS, Sigma) in sterile PBS. Mice were euthanized after 96 hours, and $CD90.1^+$ OT-II cells were analyzed via flow cytometry from single cell suspensions of splenocytes as described below.

Bulk RNA-seq and transcriptomics

Total RNA was extracted from immunomagnetic-separated $CD4^+$ T cells derived from spleens of control (nontumor-bearing) and lymphoma-bearing C57BL/6J ($CD45.2^+$) mice 7 or 14 days after transplant using the manufacturer's protocol for Nucleospin RNA Kits (Macherey-Nagel). Extracted RNA was screened for quality, and most samples had RIN values >8 on an Agilent TapeStation RNA ScreenTape (Agilent Technologies) and were fluorometrically quantified using the Qubit RNA BR Assay Kit (Thermo Fisher Scientific). The samples were then processed for RNA-seq using the NuGen Universal RNA-seq with Mouse AnyDeplete System (NuGen, Inc.).

Briefly, 100 ng of RNA was used to generate double-stranded cDNA and a ribosomal RNA-depleted strand-specific library following the manufacturer's protocol (Universal RNA-Seq Library Preparation Kit; Tecan). Quality control steps included TapeStation library assessment and qPCR for library quantification. The libraries were then sequenced on the Illumina NextSeq 2000 sequencer with a 2 × 55-base paired-end sequencing run. RNA-seq reads were then mapped against mouse genome mm10 using STAR-2.5.3a (29). Gene-level quantification was then determined with HTSeq 0.6.1 (30) using the mm10_refGene_okID.gtf gene model [downloaded from the University of California Santa Crus (UCSC), https://hgdownload.soe.ucsc.edu/goldenPath/mm10/bigZips/genes/] by summation of raw counts of reads aligned to the region associated with each gene. Gene expression data were normalized using DESeq2_1.6.3 (31). Significantly differentially expressed genes (DEG) were identified using the following criteria: adjusted *P*-value (*P*_adj) <0.01 and absorbance (abs) ($\log_2$ fold-change) >0.585 and base mean >10.

Dataset analysis of human lymphoma samples

A normalized human diffuse large B-cell lymphoma (DLBCL) RNA-seq dataset matching the RNA-seq data used in Reddy and colleagues (EGAS00001002606; ref. 32), was provided directly from Dr. Reddy. Low and high *MYC* expression was defined using the lower and upper 25th and 75th percentiles, respectively.

Affymetrix Array data were also obtained for patients with Burkitt lymphoma (mBL) and non-Burkitt lymphoma (non-mBL) (GSE4475). RAW CEL files (33) were downloaded from GEO, normalized with IRON (34), log2-transformed, and then de-batched with ComBat (35). Data were then divided into mBL and non-mBL based on the "Molecular.Diagnosis" field in the GSE4475 associated series matrix file. Genes of interest were chosen based on similar genes analyzed in the mouse CD4$^+$ T-cell dataset described above.

Metabolomics

Reagents and chemicals

Ammonium hydroxide and ammonium carbonate were obtained from MilliporeSigma. LC/MS grade solvents, including water, methanol, and acetonitrile, were purchased from Burdick and Jackson (Honeywell, sourced via VWR). The Metabolomics Quality Control (QC) Kit, which contains 14 stable isotope-labeled metabolite standards (Cambridge Isotope Labs), included the following compounds: L-alanine (^{13}C3, 99% purity), L-leucine (^{13}C6, 99%), L-phenylalanine (^{13}C6, 99%), L-tryptophan (^{13}C11, 99%), L-tyrosine (^{13}C6, 99%), caffeine (^{13}C3, 99%), D-glucose (^{13}C6, 99%), benzoate (^{13}C6, 99%), citrate (^{13}C3, 99%), octanoate (^{13}C8, 99%), propionate (^{13}C3, 99%), stearic acid (^{13}C18, 98%), succinic acid (^{13}C4, 99%), and D-sucrose (^{13}C6, 98%).

Ultra-high-performance liquid chromatography, high-resolution mass spectrometry chromatography

Chromatographic separation was performed using a SeQuant ZIC-pHILIC guard column (4.6 mm ID × 20 mm length, 5 μm particle size) and a SeQuant ZIC-pHILIC LC column (4.6 mm ID × 150 mm length, 5 μm particle size; MilliporeSigma). Mobile phase A was aqueous 10 mmol/L ammonium carbonate and 0.05% ammonium hydroxide, and mobile phase B was 100% acetonitrile. The gradient program included the following steps: start at 80% B, a linear gradient from 80 to 20% B over 13 minutes, stay at 20% B for 2 minutes, return to 80% B for 0.1 minute, and re-equilibration for 4.9 minutes for a total run time of 20 minutes. The flow rate was set to 0.4 mL/minute. The autosampler was cooled to 5°C, and the column temperature was set to 30°C.

Sample preparation

Cell pellets were prepared from 1 × 10^6 splenic C57BL/6J (CD45.2$^+$) CD4$^+$ T cells, from 2 × 10^6 splenic C57BL/6J (CD45.2$^+$) B cells, or from 2 × 10^6 splenic Eμ-*Myc* (CD45.2$^+$) B220$^+$ B cells from CD45.1$^+$ transplanted mice. Cells were isolated on Day 0 (nontumor-bearing controls) or 7 and 14 days after lymphoma transplant. All processes were carried out on ice. An aliquot (2 μL) of the Metabolomics QC Kit metabolite mixture was added into each sample. Aliquots of 250 μL (CD4$^+$ T cells) or 300 μL (control B cells and Eμ-*Myc* B lymphoma cells) of precooled aqueous 80% methanol extraction solvent (kept in the −80°C freezer at least 1 hour prior to extraction) were added to the samples for protein precipitation. After addition of the extraction solvent, the samples were vortexed and centrifuged at 18,800 × *g* (Microfuge 22R, Beckman Coulter) at 0°C for 10 minutes. The samples were then incubated for 30 minutes in a −80°C freezer to increase metabolite extraction. After incubation, the samples were immediately centrifuged again at 18,800 × *g* for 10 minutes at 4°C. The supernatant was then transferred to a new a microcentrifuge tube. The protein pellet was resolubilized using aqueous 20 mmol/L HEPES with 8 M urea for Bradford assays to measure the protein concentration for quality control of the samples. Dried metabolites were redissolved in 10 μL (CD4$^+$ T cells) or 15 μL (control B cells and Eμ-*Myc* lymphoma cells) aqueous 80% methanol.

Ultra-high-performance liquid chromatography, high-resolution mass spectrometry metabolomics

Ultra-high-performance liquid chromatography and high-resolution mass spectrometry was performed using a Vanquish UHPLC interfaced with a Q Exactive HF quadrupole-orbital ion trap mass spectrometer (Thermo Fisher Scientific). Chromatographic separation was performed using a SeQuant ZIC-pHILIC guard column (4.6 mm ID × 20 mm length, 5 μm particle size) and a SeQuant ZIC-pHILIC LC column (4.6 mm ID × 150 mm length, 5 μm particle size; MilliporeSigma). Mobile phase A was aqueous 10 mmol/L ammonium carbonate and 0.05% ammonium hydroxide, and mobile phase B was 100% acetonitrile. The gradient program included the following steps: start at 80% B, a linear gradient from 80 to 20% B over 13 minutes, stay at 20% B for 2 minutes, return to 80% B for 0.1 minute, and re-equilibration for 4.9 minutes, for a total run time of 20 minutes. The flow rate was set to 0.400 mL/min. The autosampler was cooled to 5°C, and the column temperature was set to 30°C. Sample injection volume was 2 μL (i.e., ∼2 × 10^5 CD4$^+$ T cells and ∼ 2.7 × 10^5 control B cells or Eμ-*Myc* lymphoma B cells) for both positive ion mode and negative ion mode electrospray ionization. Full MS was performed in positive and negative mode separately, detecting ions from *m*/*z* 65 to *m*/*z* 900. In addition, data-dependent acquisition was used for MS-MS of analytes in the pooled samples to enable verification of selected metabolites and confirm assignments.

Metabolomics data analysis

MZmine software (36), version 3.53, was used to identify and quantify metabolites by matching by *m*/*z* and retention time (RT) to an in-house library containing both RT and *m*/*z* from ∼600 small molecule metabolites in a format of 96-well plates (Mass Spectrometry Metabolite Library; Sigma Aldrich, catalog no.: MSMLS). The RTs are obtained using the same instrument method, and solvents and columns are as in all the other metabolomics analyses. A batch file was used to automate the following modules: centroid mass detection, automated data analysis pipeline (ADAP) chromatogram builder (with five scans minimum group size and group intensity threshold and minimum highest intensity set to 1.0^4); smoothing (set to 5);

deconvolution by local minimum search (with chromatographic threshold 95%, 0.05 minute search minimum in RT range, 10% minimum relative height: 10%, 1.0^4 minimum absolute height, minimum peak top/edge set to 1, and 0.05–5 minutes peak duration); isotopic peak grouping (with 10 ppm *m/z* tolerance, 0.25 minute retention time tolerance, and maximum charge state); peak alignment (using *m/z* and RT tolerances from the previous step with 75% weighting for *m/z* and 25% weighting for RT); peak finder (with 10% intensity tolerance and *m/z* and RT tolerances set as in the previous steps); gap filling; duplicate peak filtering (in new average mode with *m/z* and RT tolerances as above); custom database search (using an in-house library with m/z tolerance 10 ppm and RT tolerance 0.3 minutes); adduct and complexes search; peak list row filtering; and peak list export. Peak height values were exported for further analysis.

Global scaling factor IRON (34) normalization (iron_generic–proteomics) was performed against the median sample (findmedian–Pearson) within each positive and negative ion mode dataset, separately, excluding unidentified and heavy-labeled (spike-in) rows from training, leaving heavy labeled row values unnormalized as-is. Normalized abundances were then merged into a single file and log2-transformed, converting original zero values to missing data. KEGG, HMDB, and PubChem identifiers were then automatically assigned to each row from an in-house manually curated identifier mapping database. Average values were used for metabolites with a single missing value. Annotated metabolites are provided in Supplementary Tables S1 and S2.

Pimonidazole injections

Lymphoma-bearing and control (nontumor-bearing) C57BL/6J ($CD45.2^+$) mice were injected via tail vein with 1.5 mg of pimonidazole (Hypoxyprobe). After ∼60 minutes, mice were euthanized, and spleens were processed in the absence of direct light. Single-cell suspensions were stained for flow cytometry using the eBioscience FoxP3/Transcription Factor Staining Buffer Set as described by the manufacturer (Thermo Fisher Scientific).

Flow cytometry

Flow cytometry antibody information is provided in Supplementary Table S3. Unless otherwise indicated in the figures and results, flow cytometry was primarily conducted on spleens from C57BL/6J, $CD45.1^+$, OT-1, or OT-II mice 7 or 14 days after lymphoma transplant or from control (nontumor-bearing) mice (Day 0). Up to 2×10^6 cells were placed in flow tubes and stained as follows. Antibodies to cell surface markers were added at 0.5 μL (CD4, CD8, B220, CD3 APC only, CD44, CD39, CD69, NK1.1, Tim3, MHC class I, MHC class II, PD-L1, CD45.2, PD-1, Vα2, and CD90.1) or 1 μL (CD3, CD62L, KLRG1, and CXCR3) with 1 μL of FC block per sample in FACS buffer [PBS (Thermo Fisher Scientific) plus 0.4 mmol/L EDTA (Sigma), 1% FBS (GeminiBio), and 0.25% BSA (Sigma)] for 15 minutes at 4°C in the dark. For mitochondrial and lysosomal staining, samples were first stained with 50 nmol/L MitoTracker Green, LysoTracker Deep Red, and/or MitoTracker Red or 5 μmol/L MitoSOX (all from Thermo Fisher Scientific) for 30 minutes at 37°C, followed by cell surface marker staining. Cells labeled *ex vivo* with Glu-Cy5 with similarly resuspended in 1 mL PBS with 1 μmol/L Glu-Cy5 and placed at 37°C for 30 minutes prior to cell surface staining. Samples analyzed fresh were resuspended in FACS buffer containing DAPI and assessed on the same day.

For cytokine staining, single-cell suspensions were placed in 1× cell stimulation cocktail (Tonbo, TNB-4975-UL100) in 1 mL complete media and cultured for 4 to 6 hours at 37°C. Cells were then labeled with 0.5 μL fixable viability dye in 1 mL PBS (Ghost Dye 780; Tonbo) for 15 minutes in PBS at room temperature, followed by cell surface staining. Samples were then fixed [Becton Dickinson (BD) cytofix/cytoperm] following manufacturer's protocol and placed a 4°C in the dark until analysis (no more than 7 days). On the day of analysis, samples were labeled with 1 μL of cytokine antibody for 30 minutes at 4°C prior to analysis.

For transcription factor and hypoxia staining, single-cell suspensions were labeled with a fixable viability dye, followed by cell surface markers and fixation (eBioscience Foxp3/Transcription Kit; Thermo Fisher Scientific). Fixed cells were kept at 4°C in the dark until analysis (no more than 7 days) and stained with 1 μL of transcription factor antibody or 5 μL anti-PIMO for 60 minutes at 4°C in permeabilization buffer prior to running.

Samples were refiltered with 35-μmol/L filter, and data were acquired on a BD LSRII or a BD Symphony using BD Diva software. Gating was determined by assessing control (nontumor-bearing) mice or by fluorescence minus one control. All experiments used a similar gating strategy for singlet and viability gating (Supplementary Fig. S1). Data were analyzed by FlowJo software (BD), and subsequent principal component analysis (PCA) was conducted using RStudio (https://www.rstudio.com). Samples that were analyzed at different time points or that were combined from two or more experiments were normalized to values generated from control (nontumor-bearing) mice.

Seahorse assays

Splenic $CD4^+$ T cells were isolated as described from C57BL/6J mice at 7 and 14 days following lymphoma transplant and from control (nontumor-bearing) mice. T cells were then suspended into Seahorse media [phenol-free RPMI plus 10 mmol/L glucose (Sigma), 2 mmol/L glutamine (Glutamax from Thermo Fisher Scientific), 1 mmol/L sodium pyruvate (Thermo Fisher Scientific)] and plated into a poly-D-lysine-coated Seahorse microplate at 2×10^5 cells per well. Oxygen consumption rates (OCR) and extracellular acidification rates (ECAR) of $CD4^+$ T cells were then analyzed using a Seahorse XFe96 flux analyzer before and after addition of 1 μmol/L oligomycin (Sigma) and 1.5 μmol/L carbonyl cyanide-4-(trifluoromethoxy)phenylhydrazone (FCCP, Sigma). RPMI and plates were purchased from Agilent.

ATP measurement

Splenic $CD4^+$ OT-II T cells were isolated from control (nontumor-bearing mice) or 14 days after lymphoma transplant, and splenic C57BL/6J $CD4^+$ T cells were isolated from control (nontumor-bearing) mice. Levels of ATP in immunomagnetic-selected $CD4^+$ T cells were assessed using the ATPlite Luminescence Assay System (Perkin Elmer) with 10^5 cells per replicate. Relative light units were determined as measurements of ATP using a BioTek Cytation 3 plate reader.

Microscopy

Naïve splenic $CD4^+$ T cells were isolated from lymphoma-bearing C57BL/6J mice 7 or 14 days after transplant and from control (nontumor-bearing) C57BL/6J mice, and were labeled with 200 nmol/L MitoTracker Red (Cell Signaling Technology) in PBS with 0.5% FBS, 0.5% BSA, and 2 mmol/L EDTA for 25 minutes at 37°C. Cells were then resuspended in ∼100 μL complete media and placed on a Cell-Tak-coated MatTek plate (from Corning) for 30 minutes at 37°C to settle on the plate surface. Cells were imaged using a Leica SP8 confocal microscope using the same setting across all experimental groups.

Synthesis of Glu-Cy5

Compounds for the Glu-1*N*-Cy5 intermediate and Glu-1N-Cy5 probe were synthesized according to the reported protocol in the literature (37) without any modifications (Supplementary Fig. S2).

Synthesis of the Glu-1N-Cy5 intermediate

The Cy5-carboxylic acid (10.0 mg, 0.019 mmol) was dissolved in dry dimethylformamide (DMF, 0.2 mL) under argon atmosphere in a 2.0 L round bottom flask. The 2-(1H-benzotriazole-1-yl)-1,1,3,3-tetramethylaminium tetrafluoroborate (6.80 mg, 0.0212 mmol) and triethylamine (8 μL, 0.0578 mmol) were added, and stirred 5 minutes. The 2,3,4,6-tetra-*O*-acetyl-β-D-glucopyranosylamine (8.0 mg, 0.0212 mmol) was added and stirred for 21 hours at room temperature. The reaction mixture was diluted with dichloromethane (DCM; 30 mL) and washed with water (20 mL), followed by brine (20 mL, saturated NaCl). The organic layer was separated, dried (Na_2SO_4), and concentrated under reduced pressure using a rotary evaporator. The solid obtained was purified by SiO_2 chromatography using Biotage Isolera system with 0% to 15% gradient methanol in dichloromethane to afford Glu-1N-Cy5 intermediate **1** as a blue solid (15.0 mg, 92% yield). ^{1}H NMR (500 MHz, DMSO) δ 8.63 (d, J = 9.6 Hz, 1H), 8.34 (t, J = 13.1 Hz, 2H), 7.62 (d, J = 7.4 Hz, 2H), 7.45 – 7.35 (m, 4H), 7.30 – 7.21 (m, 2H), 7.08 (m, 1H), 6.83 (d, J = 8.6 Hz, 1H), 6.57 (t, J = 12.3 Hz, 1H), 6.29 (t, J = 14.1 Hz, 2H), 5.40 – 5.29 (m, 2H), 4.89 (t, J = 9.8 Hz, 1H), 4.82 (t, J = 9.4 Hz, 1H), 4.15 (dd, J = 12.4, 4.4 Hz, 1H), 4.10 – 4.03 (m, 2H), 3.96 (dd, J = 12.4, 2.2 Hz, 1H), 3.61 (s, 3H), 2.11 (m, 2H), 1.99 (s, 3H), 1.98 (s, 3H), 1.93 (s, 3H), 1.92 (s, 3H), 1.69 (s, 14H), 1.58 – 1.49 (m, 2H), 1.42 – 1.31 (m, 2H). HRMS (ESI+): *m/z* calculated for $C_{46}H_{59}N_3O_{10}$ $(M+H)^+$ 813.4195, found 813.4157; HPLC– MS (ESI+): *m/z* 812.8 [100% $(M+H)^+$].

Synthesis of the Glu-1N-Cy5 probe

The Glu-1*N*-Cy5 intermediate **1** (14.0 mg, 0.0165 mmol) was dissolved in dry methanol (2.5 mL) in a 5 mL round bottom flask under inert conditions and sodium methoxide (6 μL of a 5.4 M solution in methanol, 0.033 mmol) and was added dropwise at 0°C. After stirring 2.5 hours at 0°C, the reaction was quenched with saturated ammonium chloride (2.0 mL) and concentrated under reduced pressure using a rotary evaporator. The residue obtained was dissolved in dichloromethane (25 mL) and washed with water (20 mL). The organic layer was separated, dried (Na_2SO_4), and concentrated under reduced pressure using a rotary evaporator to afford Glu-1*N*-Cy5-probe as a bluish gray solid (9.2 mg, 81% yield). ^{1}H NMR (500 MHz, MeOD) δ 8.55 (s, 1H), 8.24 (t, J = 13.0 Hz, 2H), 7.49 (d, J = 7.4 Hz, 2H), 7.41 (t, J = 7.7 Hz, 2H), 7.33 – 7.22 (m, 4H), 6.65 (t, J = 12.2 Hz, 1H), 6.30 (d, J = 13.1 Hz, 2H), 4.10 (t, J = 7.4 Hz, 2H), 3.82 (dd, J = 11.9, 2.3 Hz, 1H), 3.69 – 3.58 (m, 4H), 3.40 (t, J = 8.9 Hz, 1H), 3.33 (d, J = 10.1 Hz, 2H), 3.25 (t, J = 9.1 Hz, 1H), 2.27 (dd, J = 14.6, 7.2 Hz, 2H), 1.82 (m, 2H), 1.73 (s, 14H), 1.56 –1.47 (m, 2H). HRMS (ESI+): *m/z* calcd for $C_{38}H_{51}N_3O_6$ $(M+H)^+$ 645.3772, found 645.3747; HPLC–MS (ESI+): *m/z* 644.9 [100% $(M+H)^+$].

Glu-Cy5 treatment of mice

C57BL/6J mice were injected with 100 μL of 500 μmol/L Glu-Cy5 suspended in PBS via tail vein. Mice were injected 7 or 14 days after lymphoma transplant and were compared with control (nontumor-bearing) C57BL/6J mice. Mice were euthanized 30 minutes after injection, and spleens were analyzed in single-cell suspensions via flow cytometry after cell surface staining.

Quantification, statistical analysis, and rigor

Most data were analyzed using GraphPad Prism 8. Two-way or one-way ANOVA with appropriate *post-hoc* tests were used, as indicated in the figure legends. A *t* test was used to analyze experiments with two groups. A $P < 0.05$, $P_{adjusted} < 0.05$, or FDR < 0.05 was considered statistically significant. PCA using the prcomp feature in Rv3.6.0 was used to analyze some flow cytometry data. Metabolomics data were analyzed with Metaboanalyst 5.0 (38). RNA-seq data were analyzed using MATLAB (R2020a). All experiments, excluding our initial PCA and -omics experiments, were replicated at least twice.

Data availability

The data were generated by the authors. RNA-seq data have been deposited in the Gene Expression Omnibus under accession ID GSE183693. The analyzed metabolomics data are provided as supplementary tables. Other data are available from the corresponding author upon reasonable request.

Results

Early infiltration of hematopoietic tissues by highly energetic lymphoma cells

To assess the potential effects of Myc-driven lymphoma on immune surveillance, we used an Eμ-*Myc* mouse B-lymphoma transplant model (**Fig. 1A**). In this model, lymphoma progresses rapidly, where low numbers of B220$^+$ lymphoma cells are detected in secondary hematopoietic tissues 7 days after injection and create a large tumor burden by 14 days, as evidenced by increases in lymphoma cells in the peripheral blood and splenomegaly (**Fig. 1B**; Supplementary Figs. S4A–S4D).

We first confirmed that Eμ-*Myc* lymphoma cells exhibited hallmarks of Myc expression *in vivo*. As expected (39, 40), both early (day 7) and late (day 14) posttransplant splenic Eμ-*Myc* lymphoma cells were larger and had more mitochondrial biomass than normal splenic B cells (**Fig. 1C** and **D**). However, Eμ-*Myc* lymphoma cells that infiltrated the spleen early during disease were significantly larger and were endowed with more mitochondrial mass than those present late in disease. Eμ-*Myc* lymphoma cells also had reduced expression of cell surface MHC class I and PD-L1 protein than normal B cells, concordant with studies showing Myc dampens antitumor immunity (refs. 12, 41, 42; Supplementary Figs. S4E and S4F). Splenic Eμ-*Myc* lymphoma cells uniformly expressed higher MHC class II protein than normal splenic B cells (Supplementary Fig. S4G).

Untargeted metabolomics analyses revealed that infiltrating Eμ-*Myc* lymphoma cells had significantly altered metabolite pools versus normal splenic B cells (**Fig. 1E** and **F**), with significantly reduced upstream and increased downstream glycolytic intermediates (**Fig. 1G**), as has been observed for *Myc*-expressing cells *in vitro* (3, 43, 44). Pyruvate and lactate were significantly reduced in Eμ-*Myc* lymphoma cells, which could reflect shuttling pyruvate to other pathways and/or increased lactate export due to overexpression of monocarboxylate transporters (3). Eμ-*Myc* lymphoma cells also exhibited reduced levels of glutamine, likely due to Myc-driven glutaminolysis (2, 4), and had increased TCA cycle intermediates, including citrate, isocitrate, and α-ketoglutarate, compared with normal splenic B cells (**Fig. 1G**). Collectively, these findings suggest that Myc-driven lymphoma cells rapidly utilize metabolites for anaplerotic reactions *in vivo*.

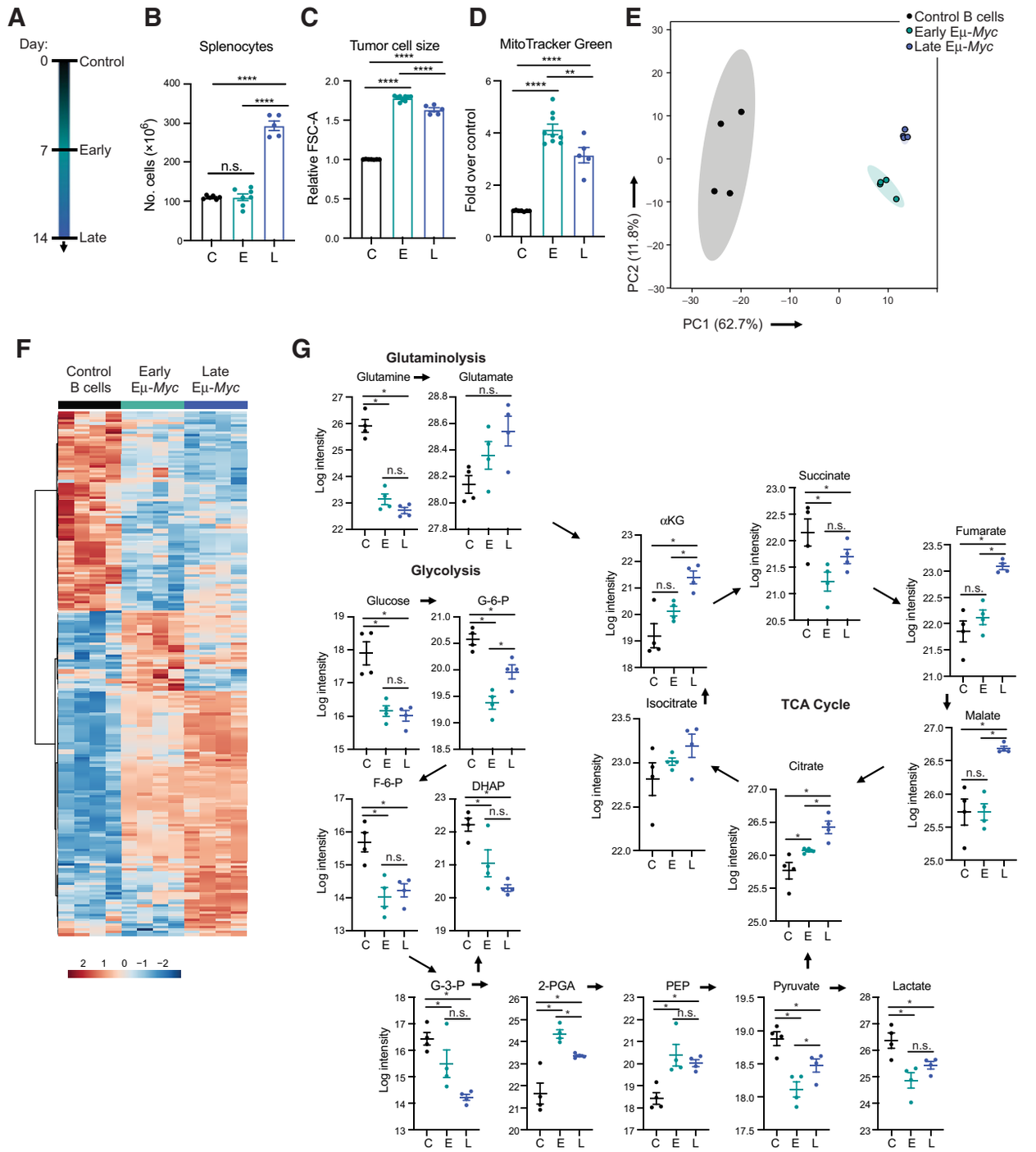

Figure 1.

Energetics of Eμ-*Myc* lymphoma cells during disease progression. **A,** Time schematic of when Eμ-*Myc* lymphoma-bearing C57BL/6J mice were analyzed following transplant; control (C, day 0), early (E, day 7), and late (L, day 14). **B,** Total splenocyte number ($n = 5$–7 mice) from Eμ-*Myc* lymphoma-bearing mice. **C,** Tumor cell size and (**D**) mitochondrial biomass, measured by flow cytometry, of Eμ-*Myc* lymphoma cells versus normal splenic B cells ($n = 5$–9 mice). **E,** PCA and (**F**) heat map of differentially abundant metabolites of Eμ-*Myc* lymphoma cells derived from spleens, at the indicated time points following lymphoma transplant, versus normal splenic B cells using untargeted metabolomics analysis ($n = 4$ mice/cohort). **G,** Levels of select metabolites in the glutaminolysis and glycolysis pathways, and in the TCA cycle, from the metabolomics data. αKG, alpha-ketoglutarate; G-6-P, glucose-6-phosphate; F-6-P, fructose-6-phosphate; DHAP, dihydroxyacetone phosphate; G-3-P, glyceraldehyde-3-phosphate; 2-PGA, 2-phosphoglyceric acid. Experiments in **B** to **D** were analyzed by one-way ANOVA and Dunnett multiple comparisons and were two independent experiments combined. Metabolomics data in **E** to **G** were analyzed using PCA and ANOVA in Metaboanalyst. Each dot indicates a biologically independent sample, and all data are mean ± SEM (*, $P < 0.05$; **, $P < 0.01$; ***, $P < 0.001$; ****, $P < 0.001$; n.s., not significant; for **G**, *, FDR < 0.05).

CD4$^+$ T cells are selectively polarized late during lymphoma progression

To determine if there were changes in the adaptive immune system during lymphoma progression, cell surface markers associated with activation or exhaustion of natural killer (NK) cells, CD4$^+$ T cells, and CD8$^+$ T cells were assessed in the bone marrow, lymph nodes (LN), and spleens from Eμ-*Myc* lymphoma-transplanted mice at early and late disease points (**Fig. 2A**). Changes in cell surface protein expression occurred in all three lymphocyte populations and across all lymphoma-bearing tissues (Supplementary Figs. S5A–S5I), and PCA revealed that

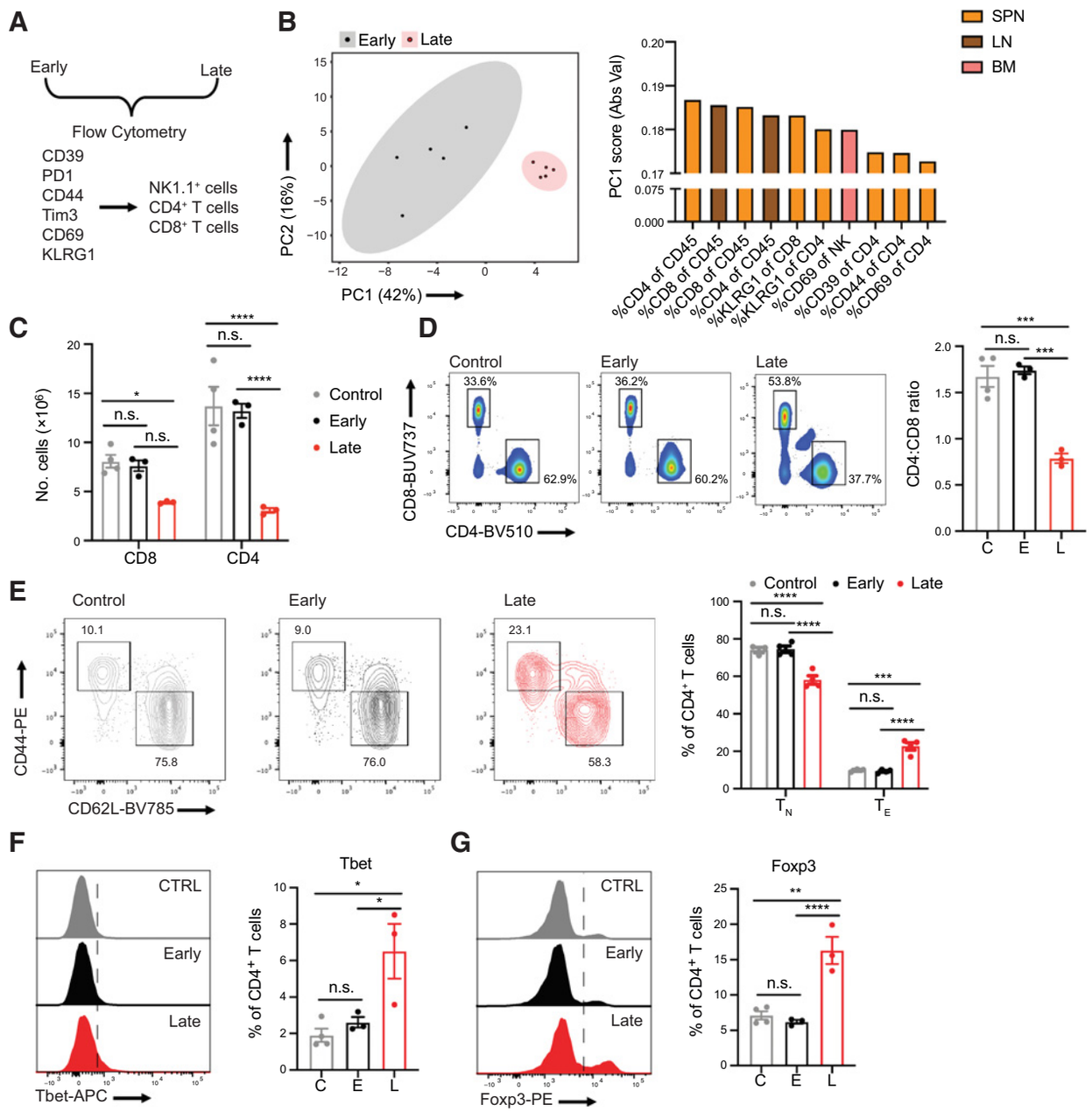

Figure 2.

Selective regulation of CD4$^+$ T-cell phenotypes late during Eμ-*Myc* lymphoma progression. **A,** Markers used for analyzing populations of NK cells (NK1.1$^+$), CD8$^+$ T cells, and CD4$^+$ T cells in Eμ-*Myc* lymphoma-bearing C57BL/6J mice by flow cytometry at the indicated time points. C, control; E, early; L, late. **B,** PCA with top 10 PC1 loading values of flow cytometry data outlined in **A** in spleen (SPN), lymph nodes (LN), and bone marrow (BM; $n = 5$ mice). **C,** Absolute number of CD8$^+$ T cells and CD4$^+$ T cells derived from control and Eμ-*Myc* lymphoma-bearing spleens ($n = 3$–4 mice). **D,** CD4:CD8 ratio and an example of CD4 versus CD8 gating, (**E**) CD44 and CD62 L flow cytograms identifying CD4$^+$ T_N (naïve) and T_E (effector) populations, and (**F**, **G**) transcription factor histograms and expression of (**F**) T-bet and (**G**) Foxp3 in CD4$^+$ T cells, as determined by flow cytometry ($n = 3$–4 mice). Experiments in **C** and **E** were analyzed by two-way ANOVA and Tukey multiple comparisons; experiments in **D**, **F**, **G** were analyzed by one-way ANOVA and Dunnett multiple comparisons. Each dot indicates a biologically independent sample; data shown are mean ± SEM. **C–G,** represent at least two independent experiments (*, $P < 0.05$; **, $P < 0.01$; ***, $P < 0.001$; n.s., not significant).

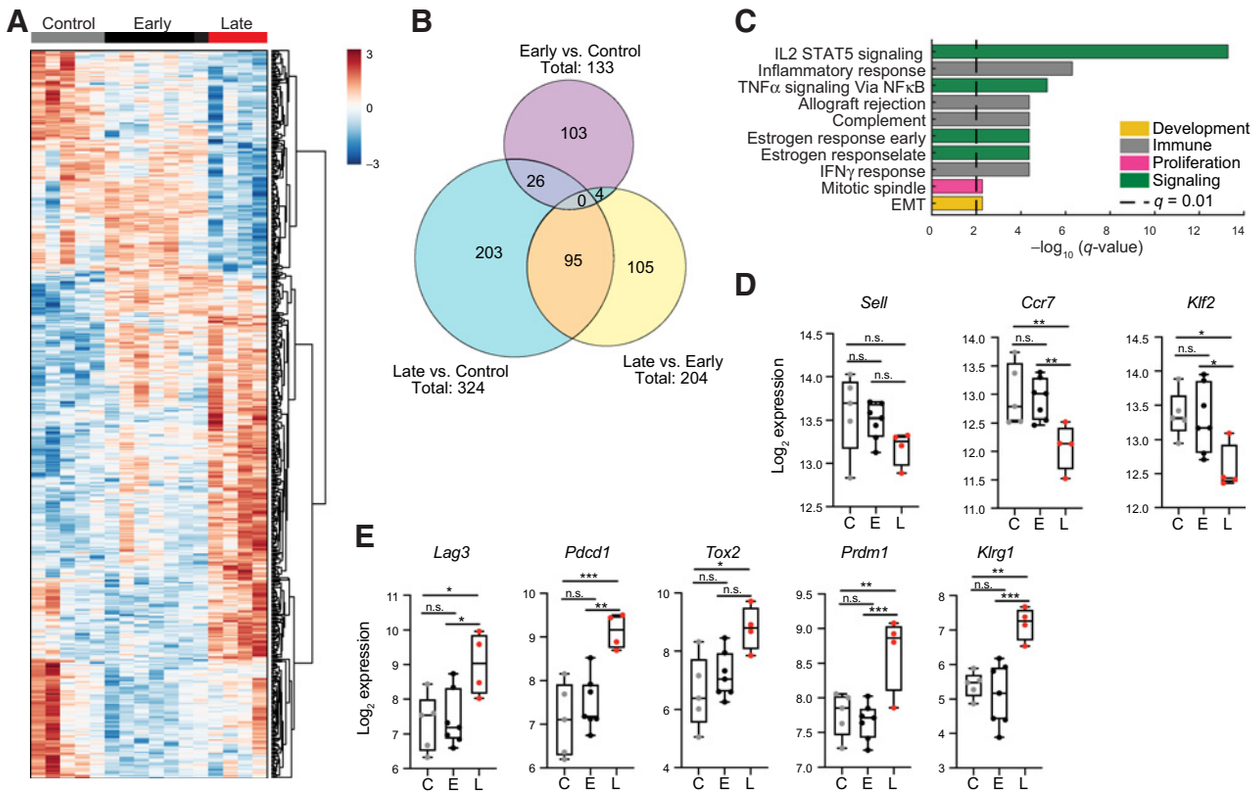

Figure 3.

Eμ-*Myc* lymphoma-derived CD4$^+$ T cells undergo transcriptional reprogramming late during disease progression. **A,** Heatmap of 536 DEG transcripts ($n = 4$–7 mice) in Eμ-*Myc* lymphoma-bearing C57BL/6J mice at the indicated timepoints. C, Control; E, early; L, late. **B,** Venn diagram of DEGs according to the indicated comparisons. **C,** Significant HALLMARK pathways for the 95 DEGs shared by Control versus Late and Early versus Late comparisons. **D** and **E,** Transcripts associated with (**D**) naïve and (**E**) exhausted T-cell phenotypes. Data shown in **D** and **E** are represented by box with 25th to 75th percentile and a line at the median and whiskers with min to max. Each dot indicates a biologically independent sample, and significance was determined by DESeq (*, $P_{adjusted} < 0.05$; **, $P_{adjusted} < 0.01$; ***, $P_{adjusted} < 0.001$; n.s., not significant).

samples separated between early versus late tumor growth (**Fig. 2B**). Features that separated PC1 were mostly specific to CD4$^+$ T cells, with a few populations of CD8$^+$ T cells also changing during lymphoma progression (**Fig. 2B**). Holm–Sidak analysis confirmed that significant differences were dominated by changes to CD4$^+$ T-cell populations (Supplementary Fig. S5J).

To define the temporal cascade of phenotypic changes to CD4$^+$ T cells during lymphoma progression, we analyzed normal CD4$^+$ T cells versus those derived from early and late lymphoma-bearing mice. Loss of total splenic CD4$^+$ T-cell numbers, as well as of CD8$^+$ T cells, was not significant until late in tumor growth (**Fig. 2C**). Consistent with our initial screen of immune populations (**Fig. 2A** and **B**), CD4$^+$ T-cell numbers were substantially more reduced than CD8$^+$ T cells, resulting in a significant decrease in the CD4:CD8 T-cell ratio that occurred only late during disease (**Fig. 2C** and **D**). Increases in the expression of KLRG1, PD-1, CD39, CD44, and CD69 among CD4$^+$ T cells were largely restricted to late phases of disease (Supplementary Fig. S6A), as was a reduction in the expression of CD62L, a marker of longevity for both naïve cells and memory T cells (Supplementary Fig. S6B). These results indicate that activation and exhaustion markers accumulate in CD4$^+$ T cells in late stages of lymphoma progression.

Activated CD4$^+$ T cells can undergo differentiation into several subtypes, including effector Th1 and Th2 cells, effector or immunosuppressive Th17 cells, and immunosuppressive regulatory T cells (Treg; ref. 45). Flow cytometry analyses revealed that CD4$^+$ T cells manifested late during lymphoma progression included CD44$^+$CD62L^{neg} effector (T_E) cells, whereas there were reductions in CD44^{neg}CD62L$^+$ naïve (T_N) cells (**Fig. 2E**). To define CD4$^+$ T-cell subsets present during early and late stages of lymphoma progression, we analyzed the expression of the transcription factors that define Th1 (T-bet), Th2 (Gata3), Th17 (RORγt), and Tregs (Foxp3). In accordance with clinical data (46–48), these analyses revealed that splenic CD4$^+$ T cells manifested late in disease expressed T-bet and Foxp3, suggesting lymphoma drives Th1 and Treg differentiation (**Fig. 2F** and **G**). CXCR3 expression, a chemokine receptor associated with Th1-cell phenotypes (49), was also induced among CD4$^+$ T cells late in disease (Supplementary Fig. S6C). These cells also exhibited elevated IFNγ production, indicating that the lymphoma-associated Th1 phenotype was functional (Supplementary Fig. S6D). Although some Gata3$^+$CD4$^+$ Th2 cells were also detected at day 14, these only represented ∼1% of the total CD4$^+$ T-cell population, and RORγt expression and IL17 production were not altered during lymphoma progression (Supplementary Figs. S6D–S6F). Collectively, these findings suggest increases in lymphoma burden polarize naïve CD4$^+$ T cells towards Th1 and Treg differentiation.

Transcriptional reprogramming of CD4$^+$ T cells occurs late during lymphoma progression

Although most phenotypic changes to CD4$^+$ T cells were observed only during late stages of lymphoma progression, we reasoned that transcriptional changes in CD4$^+$ T cells might occur early during disease. Splenic CD4$^+$ T cells isolated early and late following Eμ-*Myc* lymphoma transplant were subjected to bulk RNA-seq and compared with control splenic CD4$^+$ T cells (day 0). These analyses revealed that Th1 and Treg differentiation primarily occurred late in disease, where, for example, increased expression of *Cxcr3* and *Il12rb*, two transcripts associated with Th1 cells, were significant only among CD4$^+$ T cells present in late stages of disease (Supplementary Fig. S7A). Similarly, increased expression of several Treg-associated transcripts, specifically *Foxp3*, *Socs2*, and *Ikzf1*, was only significant among CD4$^+$ T cells isolated from spleens late during disease (Supplementary Fig. S7B).

By comparing the three groups of CD4$^+$ T cells, 536 DEGs were identified (**Fig. 3A** and **B**). Of these, ∼75% of DEGs were observed in CD4$^+$ T cells derived from late lymphoma growth, and 95 DEGs were similar between Control versus Late, as well as between Early versus Late cohorts (**Fig. 3B**). Hallmark pathway analysis of the 95 DEGs that occurred late during lymphoma progression revealed an association with T-cell activation (**Fig. 3C**). The DEGs unique to Control versus Late and to Early versus Late comparisons were also similarly associated with T-cell activation (Supplementary Figs. S7C and S7D). Pathway analysis of DEGs found early in lymphoma growth also revealed associations with some immune-related pathways (Supplementary Fig. S7E). However, the individual DEGs driving this pathway enrichment were largely decreased rather than increased, indicating some suppression of T-cell activation early during lymphoma progression (Supplementary Fig. S7F). Analysis of individual genes associated with T-cell naivety and longevity that are immediately downregulated upon TCR stimulation (50) also only occurred in CD4$^+$ T cells from late in disease (**Fig. 3D**). Finally, increased expression of several exhaustion-related transcripts, specifically *Lag3*, *Pdcd1*, *Tox2*, *Prdm1* and *Klrg1*, occurred only late in disease (**Fig. 3E**). Collectively, these data indicate lymphoma-provoked changes in CD4$^+$ T-cell transcription programs are mostly manifested at high tumor burden, and include hallmarks of TCR stimulation, Th1 and Treg cell differentiation, and T-cell exhaustion.

MYC expression in Burkitt lymphoma and DLBCL correlates with repressed T-cell immunity

To determine if immune-repressed phenotypes were also manifested in human B-cell lymphomas with *MYC* involvement, we assessed the immune phenotype of Burkitt lymphoma (mBL), which expresses elevated *MYC* due to *MYC*/immunoglobulin (*IGH*, *IGK* and *IGL*) gene translocations, versus patients with non-Burkitt B-cell lymphoma (non-mBL; ref. 33). mBL samples exhibited significantly less *CD3E* expression than non-mBL; thus, *MYC* overexpression associated with reduced T-cell numbers in the lymphoma microenvironment (**Fig. 4A**). Significant reductions in the Th1-associated genes *IFNG*, *TNF*, and *TBX21* and the activation-exhaustion marker *PDCD1* in mBL versus non-mBL was seen, consistent with repression of T-cell effector functions (**Fig. 4C–E** and **H**). In accordance with CD4$^+$ T-cell findings in the Eμ-*Myc* lymphoma transplant model, mBL samples expressed elevated *FOXP3* and *KLRG1* versus non-mBL samples (**Fig. 4F** and **G**), suggesting altered Treg differentiation in the TME of mBL patients.

Approximately 30% to 50% of diffuse large B-cell lymphomas (DLBCL) have *MYC* involvement (translocations or overexpression; ref. 51), and we further analyzed patients with high *MYC* expression in DLBCL versus those with low *MYC* expression (32).

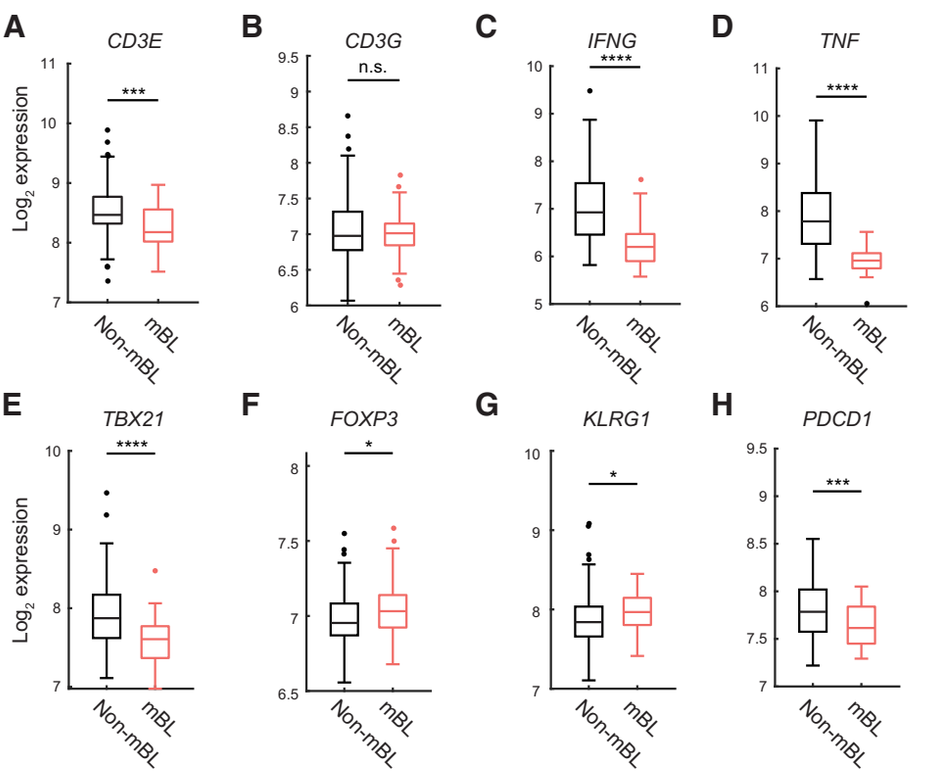

Figure 4.
Burkitt lymphoma samples exhibit reduced T-cell-associated gene transcripts. **A–H,** *CD3E*, *CD3G*, *IFNG*, *TNF*, *TBX21*, *FOXP3*, *KLRG1*, and *PDCD1* gene expression was compared in patients with Burkitt lymphoma (mBL, $n = 44$) versus those with non-Burkitt lymphoma (non-mBL, $n = 129$; ref. 33). Genes were analyzed by two-sided *t* test; box represents 25th to 75th percentile with a line at the median and the whiskers represent min to max, excluding outliers. Points are outliers if they are larger than Q3 + 1.5 × (Q3 − Q1) or smaller than Q1 − 1.5 × (Q3 − Q1), where Q1 and Q3 are the 25th and 75th percentiles, respectively (*, $P < 0.05$; ***, $P < 0.001$; ****, $P < 0.0001$; n.s., not significant).

Although DLBCL with high *MYC* expressed reduced *FOXP3* and *KLRG1* (Supplementary Figs. S8F–S8G), these lymphomas also expressed reduced *CD3E*, *CD3G*, *IFNG*, *TNF*, and *PDCD1* (Supplementary Figs. S8A–S8D and S8H). Thus, the repression of T-cell numbers is a hallmark of human B-cell lymphomas with *MYC* involvement.

Myc-driven lymphoma induces rapid mitochondrial changes in CD4$^+$ T cells

Tumor-associated T cells in both solid tumors and hematologic malignancies have impaired and reduced mitochondria (23, 52, 53), and this has been suggested to be driven by chronic TCR signaling (24), along with other processes dependent on TCR activation (54). We thus assessed if the progression of bioenergetic Eμ-*Myc* lymphoma repressed T-cell immunity via mitochondrial re-programming. Following Eμ-*Myc* lymphoma transplant, CD4$^+$ T cells exhibited a progressive early loss of mitochondrial biomass, yet most loss of mitochondrial content occurred late in disease (**Fig. 5A**). However, CD4$^+$ T cells showed an early reduction in the production of mitochondrial reactive oxygen species (ROS) following lymphoma transplant (**Fig. 5B**), and this was accompanied by a significant reduction in mitochondrial membrane potential (**Fig. 5C**). A detailed kinetic analysis of mitochondrial membrane potential versus the activation markers, CD44, CD69, and PD-1, and of the naïve marker, CD62L, revealed that significant reductions in mitochondrial membrane potential among CD4$^+$ T cells (∼Day 9) occurred before increases in the expression of activation markers or loss of naivety (∼Day 11, Supplementary Fig. S9A). Similar early reductions of mitochondrial content and ROS production were observed among lymphoma-experienced CD4$^+$ T cells derived from cervical LNs, followed by loss of mitochondrial membrane potential (Supplementary Figs. S9B–S9D).

Repressed rates of mitochondrial-associated metabolism of lymphoma-experienced CD4$^+$ T cells was confirmed by measuring oxygen consumption (OCR) under normal and stressed conditions after the addition of oligomycin and FCCP. Significant reductions in CD4$^+$

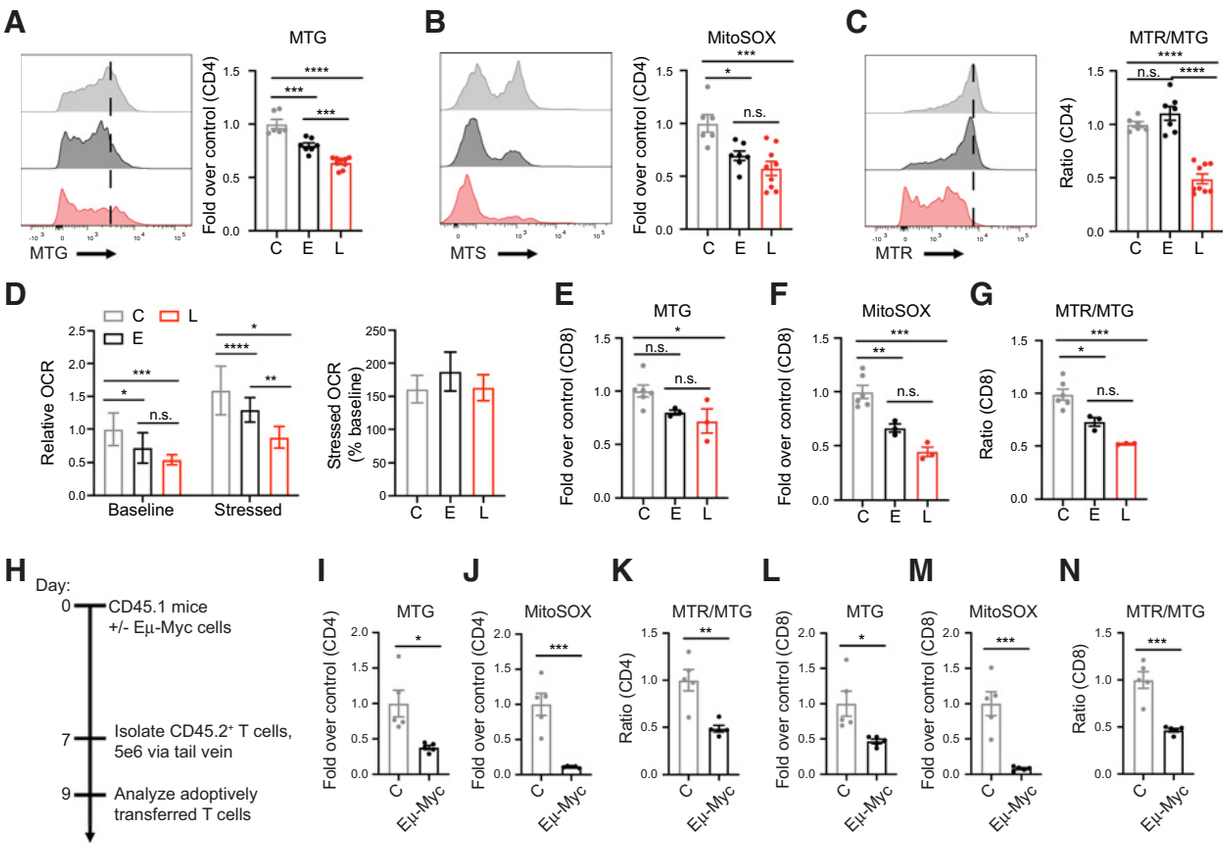

Figure 5.

T-cell mitochondrial functions are impaired early during lymphoma progression. **A,** MitoTracker Green (MTG) geometric mean fluorescence intensity (G-MFI), (**B**) MitoSOX G-MFI, and (**C**) MitoTracker Red/Green (MTR/MTG) G-MFI ratio in splenic CD4$^+$ T cells in Eμ-*Myc* lymphoma-bearing C57BL/6J mice at the indicated timepoints ($n = 6$–9 mice). C, Control; E, early; L, late. **D,** Flux analysis of OCR of splenic CD4$^+$ T cells from the indicated mice without (baseline) and with (stressed) 1 μmol/L oligomycin and FCCP. **E,** MTG G-MFI, (**F**) MitoSOX G-MFI, and (**G**) MTR/MTG G-MFI ratio in splenic CD8$^+$ T cells in Eμ-*Myc* lymphoma-bearing C57BL/6J mice at the indicated timepoints ($n = 3$–6 mice). **H,** Schematic of the experimental design used for adoptive cell transfer of T cells from nontumor-bearing C57BL/6J (CD45.2$^+$) mice into lymphoma-bearing CD45.1$^+$ mice. Mice were assessed for (**I**, **L**) MTG G-MFI, (**J**, **M**) MitoSOX G-MFI, and (**K**, **N**) MTR/MTG G-MFI ratio among adoptively transferred CD45.2$^+$ CD4$^+$ and CD8$^+$ T cells in control or Eμ-*Myc* lymphoma-bearing congenic CD45.1$^+$ mice ($n = 5$ mice). Data in **A** to **G** were analyzed by one-way ANOVA and Dunnett multiple comparisons; data in **I** to **N** were analyzed using a *t* test. Each dot in **A** to **C**, **E** to **G**, and **I** to **N** indicates a biologically independent sample; all data represent at least two independent experiments. All data are mean ± SEM, except in **H,** which is mean ± SD. Data in **A** to **C** are combined from two independent experiments (*, $P < 0.05$; **, $P < 0.01$; ***, $P < 0.001$; ****, $P < 0.0001$; n.s., not significant).

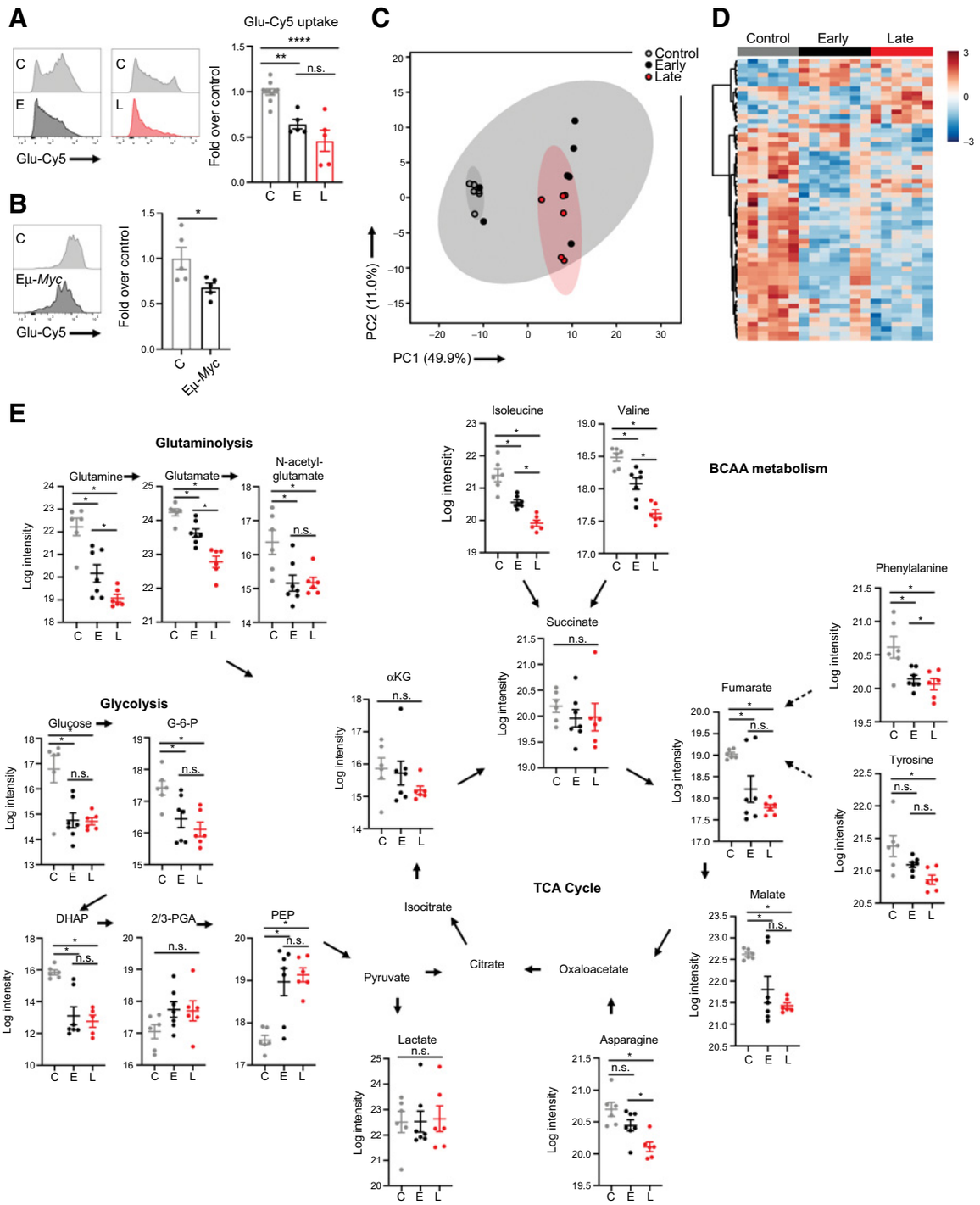

Figure 6.

Metabolic reprogramming of CD4$^+$ T cells occurs early during Eμ-*Myc* lymphoma progression. **A,** Glu-Cy5 uptake capacity in CD4$^+$ T cells from Eμ-*Myc* lymphoma-bearing C57BL/6J mice at the indicated timepoints, labeled *ex vivo* ($n = 5$–10 mice). C, Control; E, early; L, late. **B,** Glu-Cy5 uptake capacity in CD45.2$^+$ CD4$^+$ T cells transferred into normal or Eμ-*Myc* lymphoma-bearing CD45.1$^+$ congenic mice as in **Fig. 5H** ($n = 5$ mice). **C,** PCA based on untargeted metabolomics of isolated CD4$^+$ T cells from Eμ-*Myc* lymphoma-bearing C57BL/6J mice at the indicated timepoints ($n = 6$–7 mice). **D,** Heatmap of 59 metabolites that were differentially abundant by ANOVA at the indicated timepoints. **E,** Levels of select metabolites from glycolysis, glutaminolysis, the TCA cycle, and amino acid metabolism pathways that feed into the TCA cycle; G-6-P, glucose-6-phosphate; DHAP, dihydroxyacetone phosphate; 2/3-PGA, 2/3-phosphoglyceric acid; αKG, alpha-ketoglutarate. Data in **A** were analyzed by a one-way ANOVA with a Dunnett multiple comparisons; data in **B** were analyzed by a *t* test. Metabolomics data were analyzed using PCA and ANOVA in Metaboanalyst. Each dot indicates a biologically independent sample, and all data are mean ± SEM (*, $P < 0.05$; **, $P < 0.01$; ***, $P < 0.001$ in **A** and **B**. *, FDR < 0.05 in **E**; n.s., not significant).

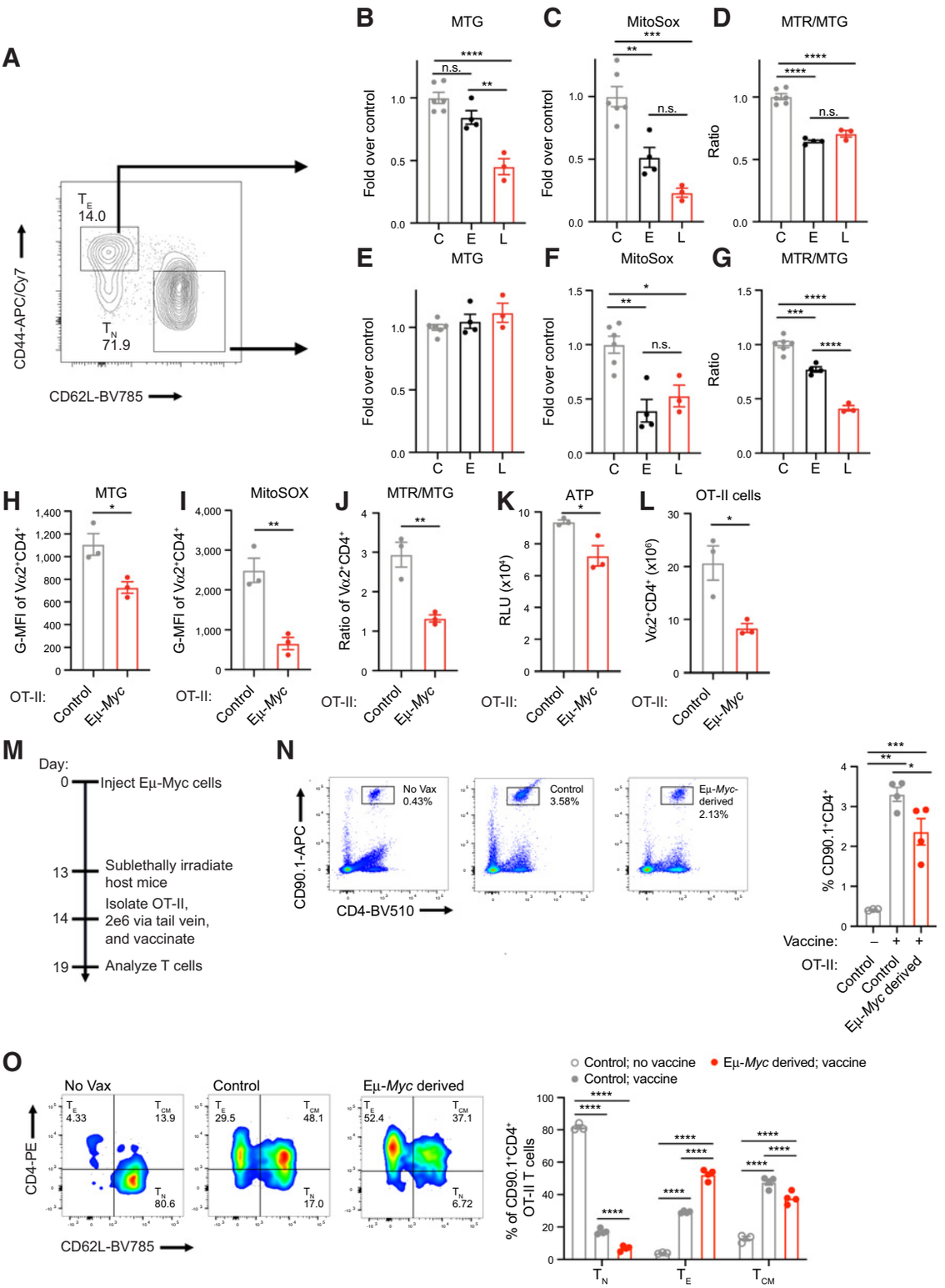
A
B
MTG
C
MitoSox
D
MTR/MTG
Fold over control
Ratio
C E L
n.s.
E
MTG
F
MitoSox
G
MTR/MTG
H
MTG
G-MFI of Vα2+CD4+
I
MitoSOX
J
MTR/MTG
Ratio of Vα2+CD4+
K
ATP
RLU (x10⁴)
L
OT-II cells
Vα2+CD4+ (x10⁶)
OT-II:
Control
Eμ-Myc
CD44-APC/Cy7
CD62L-BV785
T_E 14.0
T_N 71.9
M
Day:
0 Inject Eμ-Myc cells
13 Sublethally irradiate host mice
14 Isolate OT-II, 2e6 via tail vein, and vaccinate
19 Analyze T cells
N
No Vax 0.43%
Control 3.58%
Eμ-Myc-derived 2.13%
CD90.1-APC
CD4-BV510
% CD90.1+CD4+
Vaccine:
Control
Control
Eμ-Myc derived
O
No Vax
Control
Eμ-Myc derived
T_E 4.33
T_CM 13.9
T_N 80.6
T_E 29.5
T_CM 48.1
T_N 17.0
T_E 52.4
T_CM 37.1
T_N 6.72
CD4-PE
CD62L-BV785
Control; no vaccine
Eμ-Myc derived; vaccine
Control; vaccine
% of CD90.1+CD4+ OT-II T cells
T_N
T_E
T_CM

T-cell OCR were observed at early and late time points under both conditions (**Fig. 5D**, left). The proportional change in OCR under stressed conditions was similar across all experimental groups, indicating some mitochondrial function is retained during lymphoma growth (**Fig. 5D**, right). Conversely, ECAR rates remained below the threshold for accurate measurements in all experimental groups, even with stress, suggesting lactate-producing glycolysis is not a compensatory pathway for lymphoma-derived CD4$^+$ T cells (Supplementary Fig. S9E). Although our data and previous studies using the Eμ-*Myc* model indicate that CD8$^+$ T cells do not readily generate effector cells in response to tumor growth (Supplementary Fig. S9F; ref. 55), we found that these CD8$^+$ T cells similarly lost mitochondrial mass, membrane potential, and mitochondrial ROS during Eμ-*Myc* lymphoma progression (**Fig. 5E–G**).

The data, thus far, indicate that alterations in mitochondrial activity in lymphoma-associated T cells precedes the appearance of activation-exhaustion stages. This could be due to 7 days of exposure to expanding numbers of Eμ-*Myc* B lymphoma cells. To assess this, we adoptively transferred CD45.2$^+$ CD4$^+$ and CD8$^+$ T cells from control (non-tumor-bearing) mice into CD45.1$^+$ congenic mice 7 days after Eμ-*Myc* lymphoma transplant and assessed mitochondrial phenotypes 2 days later (**Fig. 5H**). Significant reductions in mitochondrial content, ROS production, and membrane potential were observed among CD45.2$^+$ CD4$^+$ and CD8$^+$ T cells transferred into lymphoma-bearing mice versus those transferred into nontumor-bearing congenic mice (**Fig. 5I–N**). Thus, loss of mitochondrial T-cell function occurs rapidly in response to *Myc*-driven lymphomas.

Metabolite pools are depleted early in lymphoma-associated CD4$^+$ T cells

Loss of mitochondrial membrane potential and mitochondrial ROS production in CD4$^+$ T cells in lymphoma-bearing mice could be due to several effectors that directly regulate mitochondrial function and phenotype. However, lymphoma-associated splenic CD4$^+$ T cells expressed normal levels of genes that regulate mitochondrial biogenesis, fission, and fusion (Supplementary Figs. S10A and S10B). Resting T cells engage glycolysis to produce pyruvate to support mitochondrial functions (18), and we therefore assessed if glucose uptake was impaired in these cells prior to activation. To achieve this, we synthesized a fluorescent glucose analog, Glu-Cy5, which is 10-fold more sensitive than 2-NBDG (N-(7-Nitrobenz-2-oxa-1,3-diazol-4-yl)Amino)-2-Deoxyglucose; ref. 37). Directly injecting Glu-Cy5 into lymphoma-bearing mice revealed reduced uptake only at late time points (Supplementary Fig. S10C), suggesting glucose competition occurs only late in disease, although this could also reflect effects of splenomegaly that are manifested late in disease (**Fig. 1B**). To directly address if there was nutrient competition, we attempted to isolate interstitial fluid from spleens early in disease, but this was not feasible as previously described in healthy tissues (56). When splenic CD4$^+$ T cells were immediately labeled in single-cell suspensions *ex vivo*, we observed a significant reduction in Glu-Cy5 uptake observed both early and late in disease (**Fig. 6A**). We confirmed this was not simply due to 7 days of exposure of CD4$^+$ T cells to expanding numbers of lymphoma cells, as there were comparable reductions in Glu-Cy5 uptake in T cells within 48 hours of adoptive transfer into lymphoma-bearing mice (**Figs. 5H** and **6B**). Reduced glucose uptake in lymphoma-exposed CD4$^+$ T cells was not associated with significant alterations in the expression of glycolysis-related genes, suggesting glycolytic flux was not altered (Supplementary Fig. S10D).

Given reductions in glucose uptake, we reasoned that glycolytic intermediates, or other metabolites, might be significantly reduced in lymphoma-experienced CD4$^+$ T cells. To assess this, control and lymphoma-associated splenic CD4$^+$ T cells were subjected to untargeted metabolomics, after validating that the cell isolation methods were unlikely to alter metabolites, as represented by measuring intracellular ATP in control CD4$^+$ T cells (Supplementary Fig. S10E). Principal component analyses of the metabolite changes revealed that CD4$^+$ T cells separated according to whether they were derived from lymphoma-bearing mice, regardless of disease timing (**Fig. 6C**). The levels of 59 annotated metabolites were significantly different in CD4$^+$ T cells across all groups. Of these, 30 differential metabolites were common to the Early and Late cohorts versus Control CD4$^+$ T cells (**Fig. 6D**; Supplementary Fig. S10F). Metabolic pathway analysis of these 30 metabolites revealed that the most significant alterations were in amino acid pathways and the TCA cycle (Supplementary Fig. S10G). Indeed, CD4$^+$ T cells from lymphoma-bearing mice showed reductions in intracellular glutamine, glutamate, and N-acetyl-glutamine in agreement with low mitochondrial activity, as well as a significant reduction in the branched chain amino acids isoleucine and valine (**Fig. 6E**). Several other amino acids that can fuel the TCA cycle through salvage pathways, such as phenylalanine and tyrosine, also exhibited large reductions among CD4$^+$ T cells from lymphoma-bearing mice. Key metabolites in the TCA cycle, fumarate and malate, were also reduced in CD4$^+$ T cells early during lymphoma progression, indicating early impairment of this central metabolic pathway (**Fig. 6E**). Finally, reductions in α-ketoglutarate were also manifested in CD4$^+$ T cells late following lymphoma transplant, consistent with impaired glutaminolysis during disease progression.

Analysis of glycolysis revealed that this central metabolic pathway was also disrupted in CD4$^+$ T cell by lymphoma progression. One exception was phosphoenolpyruvate (PEP), which increased in CD4$^+$ T cells from lymphoma-bearing mice (**Fig. 6E**). Increased PEP in CD4$^+$ T cells was not associated with increased expression of *Pck2*, which generates PEP from oxaloacetate (Supplementary Fig. S10D), suggesting that intracellular CD4$^+$ T-cell PEP was derived extrinsically, for example from Eμ-*Myc* lymphoma cells that also exhibited high levels of PEP (**Fig. 1G**).

Losses in amino acids and metabolic starvation in general can induce autophagic pathways, including mitophagy. However, there

Figure 7.

Eμ-*Myc* lymphoma-induced mitochondrial reprogramming of T cells is independent of TCR signaling. **A,** Gating strategy to assess CD62L$^+$CD44^{neg} T_N (naïve) and CD62L^{neg}CD44$^+$ T_E (effector) CD4$^+$ T cells from Eμ-*Myc* lymphoma-bearing C57BL/6J mice at the indicated timepoints. C: control, E: early, L: late. Mice were also assessed for (**B**, **E**) MitoTracker Green (MTG) G-MFI (geometric mean fluorescence intensity), (**C, F**) MitoSOX G-MFI, (**D**, **G**) and MitoTracker Red/Green (MTR/MTG) G-MFI ratio in effector (**B–D**) or naïve (**E–G**) CD4$^+$ T cells ($n = 3$–6 mice). **H,** MTG G-MFI, (**I**) MitoSOX G-MFI, (**J**) and MTR/MTG G-MFI ratio in splenic OT-II CD4$^+$ T cells isolated 14 days following Eμ-*Myc* lymphoma transplant ($n = 3$ OT-II mice). **K,** Relative intracellular ATP in OT-II CD4$^+$ T cells at day 14 from lymphoma-bearing mice ($n = 3$ OT-II mice). **L,** Absolute number of OT-II CD4$^+$ T cells at day 14 from control and lymphoma-bearing mice ($n = 3$ OT-II mice). **M,** Schematic of vaccination strategy using normal or lymphoma-derived OT-II CD4$^+$ T cells that were subsequently injected into C57BL/6J (CD90.2$^+$) mice and immediately vaccinated with LPS and OVA peptide. CD90.1$^+$ cells in the spleen were then analyzed 5 days later. **N** and **O,** The percent and phenotype of OT-II CD4$^+$ T cells as determined by the congenic marker in OT-II mice, CD90.1 ($n = 3$–4 mice). T_{CM}: central memory T cells. All data are mean ± SEM. Data in **B–G** and **N** were analyzed by one-way ANOVA and Dunnett's multiple comparisons; data in **H–L** were analyzed by t-test; data in **O** were analyzed by two-way ANOVA and a Tukey's test. Each dot indicates a biologically independent sample, and each panel represents at least two independent experiments. *, $P < 0.05$; **, $P < 0.01$; ***, $P < 0.001$; ****, $P < 0.0001$, n.s.: not significant.

were no significant alterations in the expression of genes that control mitophagy among lymphoma-derived $CD4^+$ T cells (Supplementary Fig. S10H). Indeed, there were significant decreases in lysosomal mass among lymphoma-derived $CD4^+$ T cells, confirming low involvement of mitophagy, and suggesting that loss of mitochondrial function may provoke lysosomal impairment of lymphoma-derived $CD4^+$ T cells (Supplementary Fig. S10I; ref. 57).

Finally, because hypoxia can impair T-cell metabolism in the TME (24), we also evaluated hypoxia in $CD4^+$ T cells by PIMO staining (58) during early and late stages of disease. There were no significant increases in PIMO among lymphoma-experienced $CD4^+$ T cells (Supplementary Fig. S10J), indicating that this was not a driver of their metabolic reprogramming during lymphoma progression.

Lymphoma-driven mitochondrial reprogramming of T cells is independent of TCR signaling

The fact that mitochondria dysfunction and reductions in associated intracellular metabolites preceded phenotypic changes to $CD4^+$ T cells during lymphoma progression, and that $CD8^+$ T cells also experienced impaired mitochondrial phenotypes without evidence of activation, suggested that metabolic reprogramming of T cells by *Myc*-driven lymphoma could occur independent of TCR engagement. To test this hypothesis, we initially analyzed the mitochondrial phenotypes of $CD62L^+CD44^{neg}$ naïve (T_N) versus $CD62L^{neg}CD44^+$ effector (T_E) $CD4^+$ T-cell populations (**Fig. 7A**). As expected, mitochondrial biomass, ROS production, and membrane potential were significantly decreased in $CD4^+$ T_E cells (**Fig. 7B–D**). Although this could be due to TCR activation in the lymphoma microenvironment, these alterations occurred earlier than activation (**Figs. 2** and **3**). Polyclonal $CD4^+$ T_N cells did not exhibit decreased mitochondrial biomass (**Fig. 7E**). However, mitochondrial ROS and membrane potential in $CD4^+$ T_N cells were significantly reduced (**Fig. 7F** and **G**, Supplementary Fig. S11A); thus, the mitochondria of unactivated $CD4^+$ T cells were altered during *Myc*-driven lymphoma progression. We observed a similar loss of mitochondrial membrane potential and ROS production in $CD8^+$ T_N cells (Supplementary Figs. S11B–S11D).

To confirm these findings we used a second, independent Eμ-*Myc* lymphoma transplant model in which comparable late-stage tumor burdens were not observed until around 21 days posttransplant (Supplementary Fig. S11E). Changes in immune phenotypes in this model were similar, with significant losses in $CD4^+$ and $CD8^+$ T cells, a reversal of the CD4:CD8 ratio, and increased $CD4^+$ T_E versus $CD8^+$ T_E cells (Supplementary Figs. S11F–S11I). Among $CD4^+$ and $CD8^+$ T_N cells, there were again significant decreases in mitochondrial ROS production and membrane potential driven by lymphoma progression, affirming that Myc-driven B-cell lymphoma could impair mitochondrial function in $CD4^+$ and $CD8^+$ T cells without TCR engagement (Supplementary Figs. S11J–S11O).

To further test this notion, we also assessed lymphoma-bearing mice carrying transgenic TCR-expressing $CD8^+$ T cells (OT-I; ref. 59) or $CD4^+$ T cells (OT-II; ref. 60) that react with ovalbumin and not with Eμ-*Myc* lymphoma antigens. To ensure that only T cells that carried the transgenic TCR were assessed, analyses were restricted to $V\alpha2^+$ cells, although these comprised >95% of the total T cells (Supplementary Figs. S11P and S11Q). Increases in lymphoma burden provoked decreases in mitochondrial biomass among OT-II $V\alpha2^+CD4^+$ T cells (**Fig. 7H**); thus, reductions in mitochondrial biomass can be induced in the absence of specific TCR activation. Lymphoma-derived OT-II $V\alpha2^+CD4^+$ T cells similarly displayed reduced mitochondrial membrane potential and ROS production (**Fig. 7I** and **J**), and exhibited significant reductions in intracellular ATP (**Fig. 7K**). Eμ-*Myc* lymphoma progression also led to significant reductions in total recoverable OT-II $CD4^+$ T cells without TCR signaling (**Fig. 7L**). Finally, although increases in lymphoma burden induced minimal changes to mitochondrial biomass among OT-I $CD8^+$ T cells, there were again significant reductions in mitochondrial ROS and membrane potential (Supplementary Figs. S11R and S11T). Thus, *Myc*-driven B-cell lymphoma can significantly impair mitochondrial functions of T cells independent of TCR signaling.

Mitochondrial function is important for memory formation of T cells (61). To determine if these TCR-independent changes led to such functional impairments, we adoptively transferred normal or lymphoma-derived OT-II $CD4^+$ T cells into new recipient mice and assessed their responses to OVA vaccination (**Fig. 7M**). Although both populations responded to vaccination, the number of lymphoma-derived OT-II $CD4^+$ T cells were significantly reduced compared with normal OT-II $CD4^+$ T cells (**Fig. 7N**). Phenotypically, these lymphoma-derived OT-II $CD4^+$ T cells exhibited significantly increased $CD62L^{neg}CD44^+$ T_E cells and impaired $CD62L^+CD44^+$ T_{CM} cells (**Fig. 7O**), further demonstrating that *Myc*-driven lymphomas can modulate T-cell fate without engaging a TCR.

Discussion

Metabolic, transcriptional, and phenotypic reprogramming of lymphocytes by tumors appears to be a hallmark of cancer (62). However, the precise mechanisms by which this occurs are not resolved, nor is it clear if there are selective and/or tumor-specific effects on immune responses. As established herein, a clear feature of *Myc*-driven B-cell lymphoma was predominant effects on $CD4^+$ T-cell effector phenotypes versus other adaptive immune cells, where increases in tumor burden reduced $CD4^+$ T-cell numbers and promoted their differentiation into Tregs, which likely contributed to immune suppression, as well as promoting, to an extent, differentiation into Th1 effector cells (46, 48). Lymphoma-induced changes to $CD4^+$ T-cell differentiation could reflect evolutionary pressure mediated by *Myc*-expressing B-cell lymphoma to help bypass $CD4^+$ T cell–directed antitumor immunity, particularly because these tumor cells express elevated MHC class II versus normal B cells. In contrast, there is perhaps less evolutionary pressure for selection on $CD8^+$ T cells, as in previous work, Eμ-*Myc* lymphoma cells express reduced MHC class I (11). Finally, immune escape in our models likely did not involve the PD-L1/PD-1 checkpoint because Eμ-*Myc* lymphoma cells expressed reduced PD-L1, in accordance with the findings of others, particularly in B-cell malignancies (11, 41, 63, 64).

Most studies investigating immune system dysfunction in cancer have centered on how chronic antigen exposure in the TME contributes to metabolic changes (24, 65). In general, these models posit that T cells immediately traffic to the tumor or do so after becoming activated in the lymph node, only to encounter hypoxia and nutrient competition in the tumor niche that limit metabolites needed for T-cell activation. In addition, chronic TCR stimulation in the tumor niche has been proposed to drive and disrupt mitochondrial membrane potential (27). However, impairment of mitochondria has been reported to occur in both proliferative and non-proliferative intratumoral $CD8^+$ T cells (23), although this model used TCR-transgenic $CD8^+$ T cells that react with tumor antigens in a high tumor burden setting. As shown here, lymphoma-induced mitochondrial dysfunction of $CD4^+$ T cells was TCR-

independent, and CD8$^+$ T cells were similarly altered by lymphoma progression without evidence of activation. Collectively, these early and TCR-independent changes to CD4$^+$ T cells in B-cell lymphoma appear due to reduced capacity for metabolite uptake. Glucose and metabolomic analyses indicated this was likely true for glucose, and for glutamine and other amino acids that drive anapleurosis. Future studies are necessary to examine the direct link between metabolite loss and mitochondrial dysfunction and how lymphoma cells impair metabolite uptake capacity among CD4$^+$ T cells in the absence of activation.

The findings presented herein established that metabolic, transcriptional, and phenotypic reprogramming were uncoupled in time, where lymphoma-provoked CD4$^+$ T-cell mitochondrial dysfunction and changes to the metabolome were manifested well before significant transcriptional and phenotypic changes occurred much later in disease. Sudden, nonlinear shifts in complex systems are often preceded by early warning signs (66). We posit that such shifts in T-cell metabolism might represent early warning signs of immune collapse within the lymphoma-immune ecosystem, marked by both mitochondrial loss and intracellular metabolite starvation. Collectively, these findings support a model where the metabolic burden on immune cells begins immediately, well before significant lymphoma outgrowth, leading to reductions in several TCA intermediates, whereas tumor cells themselves are fueling the TCA. Furthermore, the data suggest that early metabolic changes in CD4$^+$ T cells inform subsequent transcriptional and phenotypic changes that contribute to immune evasion.

The regulation of immune phenotypes includes both bottom-up and top-down control by metabolism (67). In cases of top-down regulation, the phenotype of T cells determines which metabolic pathways are dominant. In contrast, in scenarios of bottom-up regulation, environmental cues, for example available or limiting metabolites, determine how T cells differentiate or function. Given the early metabolic reprogramming and subsequent CD4$^+$ T-cell differentiation described herein, we conclude that metabolic and mitochondrial re-programming of T cells in the absence of TCR activation drives bottom-up regulation of CD4$^+$ T-cell differentiation. Consistent with this model, PEP accumulated in CD4$^+$ T cells early during lymphoma progression, and PEP is a known regulator of both Th1 effector and Treg suppressive phenotypes (22, 68), the two CD4$^+$ T-cell populations that were observed late in lymphoma progression. Given the limitations to CD4$^+$ T-cell metabolic function that occur early in lymphoma progression, our data suggest that lymphoma also limits immune cell bioenergetics that are necessary for robust antitumor responses. Lymphoma-driven constraints on nutrient resources may also explain the lack of substantial effects on CD8$^+$ T-cell and NK-cell fate, as the latter population relies on similar metabolic pathways as activated T cells (69–71).

Although most of our current understanding of cancer immunometabolism is derived from solid tumor models, some studies have examined how hematologic malignancies alter the mitochondrial function of T cells. For example, CD8$^+$ T_E cells derived from patients with chronic lymphocytic leukemia have reduced mitochondrial function (52), and our analyses of MYC-driven Burkitt lymphoma (BL) expression datasets indicated BL polarized CD4$^+$ T cells towards a Treg phenotype. Further, T_N and other T-cell subsets from patients with multiple myeloma exhibit reduced mitochondrial ROS production (53). Thus, disruption of T-cell metabolism and fate are shared features of these B/plasma-cell malignancies.

Patients with *MYC*-driven B-cell lymphoma often have worse prognosis with standard therapies such as R-CHOP (8). Emerging and approved treatments for B-cell lymphoma now include immunotherapies, including chimeric antigen receptor T-cell (CAR-T) therapies (72). Given that CAR-T therapy involves processing T cells directly from patients, our studies underscore the importance of understanding how lymphoma may shape the immune system prior to CAR-T or other immunotherapy treatment. Notably, it has been shown that naïve T cells are more effective than T_E cells when producing CAR-T cells, and this has been ascribed as being due to lack of chronic antigen-specific TCR signaling (73, 74). In the context of our study, another interpretation is that the metabolism of patient T cells is compromised by lymphoma much earlier than expected, regardless of the subpopulation, and this supports the development of immunotherapies with enhanced metabolic function. Indeed, endowing CAR-T with superior metabolic capacity is suggested to be an alternative approach to cell therapies (75). Finally, given that naïve T cells are also susceptible to metabolic and subsequent phenotypic reprogramming in *Myc*-driven B-cell lymphoma, metabolic profiling may help inform which CAR-T products will mount a long-term response.

Authors' Disclosures

R.S. Hesterberg reports grants from NCI/NIH and other support from Cortner-Couch Endowed Chair for Cancer Research during the conduct of the study. J.M. Koomen reports grants from NCI during the conduct of the study; other support from Bristol Myers Squibb outside the submitted work. H.R. Lawrence reports grants from NIH/NCI during the conduct of the study. J.L. Cleveland reports grants from NCI/NIH, other support from Cortner-Couch Endowed Chair for Cancer Research from the University of South Florida, and other support from State of Florida during the conduct of the study. No disclosures were reported by the other authors.

Authors' Contributions

R.S. Hesterberg: Conceptualization, formal analysis, validation, investigation, visualization, writing–original draft, writing–review and editing. **M. Liu:** Investigation, methodology. **A.G. Elmarsafawi:** Investigation. **J.M. Koomen:** Methodology. **E.A. Welsh:** Formal analysis, methodology. **S.G. Hesterberg:** Conceptualization, investigation. **S. Ranatunga:** Methodology. **C. Yang:** Investigation. **W. Li:** Investigation. **H.R. Lawrence:** Methodology. **P.C. Rodriguez:** Conceptualization, writing–review and editing. **A.E. Berglund:** Formal analysis, investigation, visualization. **J.L. Cleveland:** Conceptualization, supervision, funding acquisition, writing–original draft, writing–review and editing.

Acknowledgments

We thank Dr. Javier Pinilla-Ibarz (Moffitt Cancer Center) for providing OT-II transgenic mice; the Moffitt/USF Animal Resource Center for animal care and their assistance with lymphoma transplant studies; Sean Yoder and the Moffitt Genomics Core for their help with RNA-seq analyses; Jodi Kroeger and the Moffitt Flow Cytometry Core; the Moffitt Proteomics & Metabolomics Core; Antonio C. Ortiz and the Moffitt Analytical Microscopy Core; and the Biostatistics & Bioinformatics Shared Resource of the Moffitt Cancer Center. We also thank Dr. Sandeep Dave (Duke University) for providing access to RNA-seq dataset of DLBCL patient samples. This work was supported by grants R01 CA241713 (to J.L. Cleveland), by the Cortner-Couch Endowed Chair for Cancer Research from the University of South Florida School of Medicine (to J.L. Cleveland), and by monies from Mr. Ted Couch to support this project. (to J.L. Cleveland). R.S. Hesterberg is a postdoctoral fellow of the T32 CA233399 program. H.R. Lawrence was supported by R50 CA211447. These studies were also supported in part by the H. Lee Moffitt Cancer Center & Research Institute, by NCI Comprehensive Cancer Center Grant No. P30 CA076292, and by support from the State of Florida to the H. Lee Moffitt Cancer Center & Research Institute.

The publication costs of this article were defrayed in part by the payment of publication fees. Therefore, and solely to indicate this fact, this article is hereby marked "advertisement" in accordance with 18 USC section 1734.

Note

Supplementary data for this article are available at Cancer Immunology Research Online (http://cancerimmunolres.aacrjournals.org/).

Received September 27, 2021; revised May 9, 2022; accepted August 3, 2022; published first August 15, 2022.

References

1. Karube K, Campo E. MYC alterations in diffuse large B-cell lymphomas. Semin Hematol 2015;52:97–106.
2. Wise DR, DeBerardinis RJ, Mancuso A, Sayed N, Zhang XY, Pfeiffer HK, et al. Myc regulates a transcriptional program that stimulates mitochondrial glutaminolysis and leads to glutamine addiction. Proc Nat Acad Sci U S A 2008;105:18782–7.
3. Doherty JR, Yang C, Scott KE, Cameron MD, Fallahi M, Li W, et al. Blocking lactate export by inhibiting the Myc target MCT1 disables glycolysis and glutathione synthesis. Cancer Res 2014;74:908–20.
4. Gao P, Tchernyshyov I, Chang TC, Lee YS, Kita K, Ochi T, et al. c-Myc suppression of miR-23a/b enhances mitochondrial glutaminase expression and glutamine metabolism. Nature 2009;458:762–5.
5. Lewis BC, Prescott JE, Campbell SE, Shim H, Orlowski RZ, Dang CV. Tumor induction by the c-Myc target genes rcl and lactate dehydrogenase A. Cancer Res 2000;60:6178–83.
6. Le A, Lane AN, Hamaker M, Bose S, Gouw A, Barbi J, et al. Glucose-independent glutamine metabolism via TCA cycling for proliferation and survival in B cells. Cell Metab 2012;15:110–21.
7. Fernandez MR, Schaub FX, Yang C, Li W, Yun S, Schaub SK, et al. Disrupting the MYC-TFEB circuit impairs amino acid homeostasis and provokes metabolic anergy. Cancer Res 2022;82:1234–50.
8. Savage KJ, Johnson NA, Ben-Neriah S, Connors JM, Sehn LH, Farinha P, et al. MYC gene rearrangements are associated with a poor prognosis in diffuse large B-cell lymphoma patients treated with R-CHOP chemotherapy. Blood 2009;114:3533–7.
9. Guo B, Tan X, Ke Q, Cen H. Prognostic value of baseline metabolic tumor volume and total lesion glycolysis in patients with lymphoma: a meta-analysis. PLoS One 2019;14:e0210224.
10. Böttcher M, Baur R, Stoll A, Mackensen A, Mougiakakos D. Linking immunoevasion and metabolic reprogramming in B-cell-derived lymphomas. Front Oncol 2020;10:594782.
11. de Jonge AV, Mutis T, Roemer MGM, Scheijen B, Chamuleau MED. Impact of MYC on anti-tumor immune responses in aggressive B cell non-hodgkin lymphomas: consequences for cancer immunotherapy. Cancers 2020;12:3052.
12. Bernards R, Dessain SK, Weinberg RA. N-myc amplification causes down-modulation of MHC class I antigen expression in neuroblastoma. Cell 1986;47:667–74.
13. God JM, Cameron C, Figueroa J, Amria S, Hossain A, Kempkes B, et al. Elevation of c-MYC disrupts HLA class II-mediated immune recognition of human B cell tumors. J Immunol 2015;194:1434–45.
14. Casey SC, Tong L, Li Y, Do R, Walz S, Fitzgerald KN, et al. MYC regulates the antitumor immune response through CD47 and PD-L1. Science 2016;352:227–31.
15. Lee YS, Heo W, Son CH, Kang CD, Park YS, Bae J. Upregulation of Myc promotes the evasion of NK cell-mediated immunity through suppression of NKG2D ligands in K562 cells. Mol Med Rep 2019;20:3301–7.
16. Liu X, Pu Y, Cron K, Deng L, Kline J, Frazier WA, et al. CD47 blockade triggers T cell-mediated destruction of immunogenic tumors. Nat Med 2015;21:1209–15.
17. Rehm A, Gätjen M, Gerlach K, Scholz F, Mensen A, Gloger M, et al. Dendritic cell-mediated survival signals in Eμ-Myc B-cell lymphoma depend on the transcription factor C/EBPβ. Nat Commun 2014;5:5057.
18. Menk AV, Scharping NE, Moreci RS, Zeng X, Guy C, Salvatore S, et al. Early TCR signaling induces rapid aerobic glycolysis enabling distinct acute T cell effector functions. Cell Rep 2018;22:1509–21.
19. Carr EL, Kelman A, Wu GS, Gopaul R, Senkevitch E, Aghvanyan A, et al. Glutamine uptake and metabolism are coordinately regulated by ERK/MAPK during T lymphocyte activation. J Immunol 2010;185:1037–44.
20. Castellano F, Molinier-Frenkel V. Control of T-cell activation and signaling by amino-acid catabolizing enzymes. Front Cell Dev Biol 2020;8:613416.
21. Chang CH, Qiu J, O'Sullivan D, Buck MD, Noguchi T, Curtis JD, et al. Metabolic competition in the tumor microenvironment is a driver of cancer progression. Cell 2015;162:1229–41.
22. Ho PC, Bihuniak JD, Macintyre AN, Staron M, Liu X, Amezquita R, et al. Phosphoenolpyruvate is a metabolic checkpoint of anti-tumor T cell responses. Cell 2015;162:1217–28.
23. Scharping NE, Menk AV, Moreci RS, Whetstone RD, Dadey RE, Watkins SC, et al. The tumor microenvironment represses T cell mitochondrial biogenesis to drive intratumoral T cell metabolic insufficiency and dysfunction. Immunity 2016;45:374–88.
24. Scharping NE, Rivadeneira DB, Menk AV, Vignali PDA, Ford BR, Rittenhouse NL, et al. Mitochondrial stress induced by continuous stimulation under hypoxia rapidly drives T cell exhaustion. Nat Immunol 2021;22:205–15.
25. Cong J, Wang X, Zheng X, Wang D, Fu B, Sun R, et al. Dysfunction of natural killer cells by FBP1-induced inhibition of glycolysis during lung cancer progression. Cell Metab 2018;28:243–55.
26. Gupta S, Roy A, Dwarakanath BS. Metabolic cooperation and competition in the tumor microenvironment: implications for therapy. Front Oncol 2017;7:68.
27. Yu YR, Imrichova H, Wang H, Chao T, Xiao Z, Gao M, et al. Disturbed mitochondrial dynamics in CD8(+) TILs reinforce T cell exhaustion. Nat Immunol 2020;21:1540–51.
28. Adams JM, Harris AW, Pinkert CA, Corcoran LM, Alexander WS, Cory S, et al. The c-myc oncogene driven by immunoglobulin enhancers induces lymphoid malignancy in transgenic mice. Nature 1985;318:533–8.
29. Dobin A, Davis CA, Schlesinger F, Drenkow J, Zaleski C, Jha S, et al. STAR: ultrafast universal RNA-seq aligner. Bioinformatics 2013;29:15–21.
30. Anders S, Pyl PT, Huber W. HTSeq—a Python framework to work with high-throughput sequencing data. Bioinformatics 2015;31:166–9.
31. Love MI, Huber W, Anders S. Moderated estimation of fold change and dispersion for RNA-seq data with DESeq2. Genome Biol 2014;15:550.
32. Reddy A, Zhang J, Davis NS, Moffitt AB, Love CL, Waldrop A, et al. Genetic and functional drivers of diffuse large B cell lymphoma. Cell 2017;171:481–94.
33. Hummel M, Bentink S, Berger H, Klapper W, Wessendorf S, Barth TF, et al. A biologic definition of Burkitt's lymphoma from transcriptional and genomic profiling. N Engl J Med 2006;354:2419–30.
34. Welsh EA, Eschrich SA, Berglund AE, Fenstermacher DA. Iterative rank-order normalization of gene expression microarray data. BMC Bioinf 2013;14:153.
35. Johnson WE, Li C, Rabinovic A. Adjusting batch effects in microarray expression data using empirical Bayes methods. Biostatistics 2007;8:118–27.
36. Pluskal T, Castillo S, Villar-Briones A, OM MZmine. 2: modular framework for processing, visualizing, and analyzing mass spectrometry-based molecular profile data. BMC Bioinf 2010;11:395.
37. Xu H, Liu X, Yang J, Liu R, Li T, Shi Y, et al. Cyanine-based 1-amino-1-deoxyglucose as fluorescent probes for glucose transporter mediated bioimaging. Biochem Biophys Res Commun 2016;474:240–6.
38. Pang Z, Chong J, Zhou G, de Lima Morais DA, Chang L, Barrette M, et al. MetaboAnalyst 5.0: narrowing the gap between raw spectra and functional insights. Nucleic Acids Res 2021;49:W388–w96.
39. Li F, Wang Y, Zeller KI, Potter JJ, Wonsey DR, O'Donnell KA, et al. Myc stimulates nuclearly encoded mitochondrial genes and mitochondrial biogenesis. Mol Cell Biol 2005;25:6225–34.
40. Baena E, Gandarillas A, Vallespinós M, Zanet J, Bachs O, Redondo C, et al. c-Myc regulates cell size and ploidy but is not essential for postnatal proliferation in liver. Proc Nat Acad Sci U S A 2005;102:7286–91.
41. Elbaek MV, Pedersen M, Breinholt MF, Reddy A, Love C, Clasen-Linde E, et al. PD-L1 expression is low in large B-cell lymphoma with MYC or double-hit translocation. Hematol Oncol 2019;37:375–82.
42. Croxford JL, Tang ML, Pan MF, Huang CW, Kamran N, Phua CM, et al. ATM-dependent spontaneous regression of early Eμ-myc-induced murine B-cell leukemia depends on natural killer and T cells. Blood 2013;121:2512–21.
43. de la Cova C, Senoo-Matsuda N, Ziosi M, Wu DC, Bellosta P, Quinzii CM, et al. Supercompetitor status of Drosophila Myc cells requires p53 as a fitness sensor to reprogram metabolism and promote viability. Cell Metab 2014;19:470–83.
44. Stine ZE, Walton ZE, Altman BJ, Hsieh AL, Dang CV. MYC, metabolism, and cancer. Cancer Discov 2015;5:1024–39.
45. Zhu J, Yamane H, Paul WE. Differentiation of effector CD4 T cell populations (*). Annu Rev Immunol 2010;28:445–89.
46. Yang ZZ, Novak AJ, Stenson MJ, Witzig TE, Ansell SM. Intratumoral CD4+CD25+ regulatory T-cell-mediated suppression of infiltrating CD4+ T cells in B-cell non-Hodgkin lymphoma. Blood 2006;107:3639–46.
47. Lu T, Yu S, Liu Y, Yin C, Ye J, Liu Z, et al. Aberrant circulating Th17 cells in patients with B-cell non-Hodgkin's lymphoma. PLoS One 2016;11:e0148044.
48. Roider T, Seufert J, Uvarovskii A, Frauhammer F, Bordas M, Abedpour N, et al. Dissecting intratumour heterogeneity of nodal B-cell lymphomas at the transcriptional, genetic and drug-response levels. Nat Cell Biol 2020;22:896–906.
49. Groom JR, Luster AD. CXCR3 in T cell function. Exp Cell Res 2011;317:620–31.
50. Endrizzi BT, Jameson SC. Differential role for IL-7 in inducing lung Kruppel-like factor (Kruppel-like factor 2) expression by naive versus activated T cells. Int Immunol 2003;15:1341–8.

51. Nguyen L, Papenhausen P, Shao H. The role of c-MYC in B-cell lymphomas: diagnostic and molecular aspects. Genes 2017;8:116.
52. van Bruggen JAC, Martens AWJ, Fraietta JA, Hofland T, Tonino SH, Eldering E, et al. Chronic lymphocytic leukemia cells impair mitochondrial fitness in CD8 (+) T cells and impede CAR T-cell efficacy. Blood 2019;134:44–58.
53. Cooke RE, Quinn KM, Quach H, Harrison S, Prince HM, Koldej R, et al. Conventional treatment for multiple myeloma drives premature aging phenotypes and metabolic dysfunction in T cells. Front Immunol 2020;11:2153.
54. Song M, Sandoval TA, Chae CS, Chopra S, Tan C, Rutkowski MR, et al. IRE1α-XBP1 controls T cell function in ovarian cancer by regulating mitochondrial activity. Nature 2018;562:423–8.
55. Prato S, Mintern JD, Lahoud MH, Huang DC, Villadangos JA. Induction of antigen-specific effector-phase tolerance following vaccination against a previously ignored B-cell lymphoma. Immunol Cell Biol 2011;89:595–603.
56. Sullivan MR, Danai LV, Lewis CA, Chan SH, Gui DY, Kunchok T, et al. Quantification of microenvironmental metabolites in murine cancers reveals determinants of tumor nutrient availability. eLife 2019;8:e44235.
57. Demers-Lamarche J, Guillebaud G, Tlili M, Todkar K, Bélanger N, Grondin M, et al. Loss of mitochondrial function impairs lysosomes. J Biol Chem 2016;291:10263–76.
58. Aguilera KY, Brekken RA. Hypoxia Studies with Pimonidazole in vivo. Bio-protocol 2014;4:e1254.
59. Hogquist KA, Jameson SC, Heath WR, Howard JL, Bevan MJ, Carbone FR. T cell receptor antagonist peptides induce positive selection. Cell 1994;76:17–27.
60. Barnden MJ, Allison J, Heath WR, Carbone FR. Defective TCR expression in transgenic mice constructed using cDNA-based alpha- and beta-chain genes under the control of heterologous regulatory elements. Immunol Cell Biol 1998;76:34–40.
61. van der Windt GJ, Everts B, Chang CH, Curtis JD, Freitas TC, Amiel E, et al. Mitochondrial respiratory capacity is a critical regulator of CD8+ T cell memory development. Immunity 2012;36:68–78.
62. Leone RD, Powell JD. Metabolism of immune cells in cancer. Nat Rev Cancer 2020;20:516–31.
63. Zou J, Zhuang M, Yu X, Li N, Mao R, Wang Z, et al. MYC inhibition increases PD-L1 expression induced by IFN-γ in hepatocellular carcinoma cells. Mol Immunol 2018;101:203–9.
64. Wu X, Nelson M, Basu M, Srinivasan P, Lazarski C, Zhang P, et al. MYC oncogene is associated with suppression of tumor immunity and targeting Myc induces tumor cell immunogenicity for therapeutic whole cell vaccination. J Immunother Cancer 2021;9:e001388.
65. Vardhana SA, Hwee MA, Berisa M, Wells DK, Yost KE, King B, et al. Impaired mitochondrial oxidative phosphorylation limits the self-renewal of T cells exposed to persistent antigen. Nat Immunol 2020;21:1022–33.
66. Scheffer M, Bascompte J, Brock WA, Brovkin V, Carpenter SR, Dakos V, et al. Early-warning signals for critical transitions. Nature 2009;461:53–9.
67. Shyer JA, Flavell RA, Bailis W. Metabolic signaling in T cells. Cell Res 2020;30:649–59.
68. Watson MJ, Vignali PDA, Mullett SJ, Overacre-Delgoffe AE, Peralta RM, Grebinoski S, et al. Metabolic support of tumour-infiltrating regulatory T cells by lactic acid. Nature 2021;591:645–51.
69. Schafer JR, Salzillo TC, Chakravarti N, Kararoudi MN, Trikha P, Foltz JA, et al. Education-dependent activation of glycolysis promotes the cytolytic potency of licensed human natural killer cells. J Allergy Clin Immunol 2019;143:346–58.
70. Marçais A, Marotel M, Degouve S, Koenig A, Fauteux-Daniel S, Drouillard A, et al. High mTOR activity is a hallmark of reactive natural killer cells and amplifies early signaling through activating receptors. eLife 2017;6:e26423.
71. Wang Z, Guan D, Wang S, Chai LYA, Xu S, Lam KP. Glycolysis and oxidative phosphorylation play critical roles in natural killer cell receptor-mediated natural killer cell functions. Front Immunol 2020;11:202.
72. Schuster SJ, Bishop MR, Tam CS, Waller EK, Borchmann P, McGuirk JP, et al. Tisagenlecleucel in adult relapsed or refractory diffuse large B-cell lymphoma. N Engl J Med 2019;380:45–56.
73. Sommermeyer D, Hudecek M, Kosasih PL, Gogishvili T, Maloney DG, Turtle CJ, et al. Chimeric antigen receptor-modified T cells derived from defined CD8+ and CD4+ subsets confer superior antitumor reactivity *in vivo*. Leukemia 2016;30:492–500.
74. McLellan AD, Ali Hosseini Rad SM. Chimeric antigen receptor T cell persistence and memory cell formation. Immunol Cell Biol 2019;97:664–74.
75. Ye L, Park JJ, Peng L, Yang Q, Chow RD, Dong MB, et al. A genome-scale gain-of-function CRISPR screen in CD8 T cells identifies proline metabolism as a means to enhance CAR-T therapy. Cell Metab 2022;34:595–614.